Challenges of Field Inhomogeneities and a Method for Compensation

A DISSERTATION
SUBMITTED TO THE FACULTY OF THE GRADUATE SCHOOL
OF THE UNIVERSITY OF MINNESOTA BY

Angela Lynn Styczynski Snyder

IN PARTIAL FULFILLMENT OF THE REQUIREMENTS
FOR THE DEGREE OF
DOCTOR OF PHILOSOPHY

Michael Garwood, Ph.D., Adviser

November 2011

Acknowledgements

First I would like to thank Michael Garwood for his guidance and support. Working for such a visionary has been a great privilege. Moreover, I would like to thank him not just for teaching me MR but for his patience and persistence in training me to grow and mature as a scientist. He taught me to present my ideas with confidence, to defend my research with eloquence, and to believe that while hard work might produce data, passion produces great science.

I would like to thank my committee Thomas Vaughan, Kamil Ugurbil, and Bruce Hammer for their advice and insight.

I am grateful to Patrick Bolan for all the work and wisdom he brought to the 7 T liver imaging and spectroscopy project. The high standards to which he consistently holds himself and his research are truly inspirational.

Many thanks are due Shalom Michaeli for the momentum and inspiration he brought to the uterus project. I greatly appreciate his enthusiasm, optimism, and encouragement.

I would like to thank the Garwood group, with particular thanks for help and support through the SWIRLY project going to Curtis Corum, Nathaniel Powell, Steen Moeller, Djaudat Idiyatullin, Michael Tesch, and Robert O'Connell.

I want express my great appreciation to Curtis Corum, Nathaniel Powell, Can Akgun, and Carl Snyder for conversations and camaraderie over many shared rounds of wings.

Thank you to everyone at CMRR. The concentration of intelligence is overwhelming.

Financial support for these projects came from BTRR - P41 RR008079, the Keck Foundation, the MIND Institute, and *Carestream Health* RSNA Research Scholar Grant.

I thank my small group for tireless prayers and positivity and John Piper and Bethlehem Baptist Church for giving me eternal perspective on my time in graduate school.

My heart-felt thanks go to Ken and Carolyn Snyder for being the most understanding and encouraging in-laws for which one could ever hope. There will never be enough words to express my gratitude to my family, Mark and Ann Styczysnki, and Nicole, Ashley, Dane, Lauren, John, and Lydia, for their cheers, consolation, and confidence. I have been abundantly blessed to be part of such a tremendously loving and supportive family. Also, I want to thank my husband Carl for being by my side every step of the way, unwavering through the best and the worst of it, and for making me smile when I needed it most.

Finally, I want to give all credit to the one to whom all glory and honor and thanksgiving are due and compared to whom a PhD is as loss. "I count everything as loss because of the surpassing worth of knowing Christ Jesus my Lord." Philipians 3:8

To Mom, Dad, Nikki, Ashley, Dane, and Lauren,
and especially Carl

Abstract

MRI of the body at 7 T has become possible only very recently. High fields bring the advantages of increased signal to noise ratio, resolution gains, faster image acquisition through better parallel imaging, improved and novel types of contrast, and greater spectral dispersion. There are many obstacles to be faced in the advancement to 7 T including field inhomogeneities, transmit inhomogeneities, and increased RF-absorption risk. Inhomogeneous B_1^+ is possibly the most significant obstacle currently facing 7 T body imaging in consistently producing clinical-quality images.

In this work, the first demonstrations of MR imaging and spectroscopy (MRS) of the liver at 7 T are presented and evaluated with special attention given to parallel imaging. Also presented here is the first demonstration of imaging of the uterus at 7 T with particular emphasis on contrast between uterine layers. A comparison was done between 3 T and 7 T, and relaxation rates were mapped including higher rotating frame relaxations.

SWIRLY **(s**patiotemporal-encoding **w**ith **i**ncremental **r**efocusing a**l**ong a trajecto**ry)** is a novel pulse sequence that employs a frequency and amplitude modulated excitation pulse in the presence of sinusoidal gradients to move a region of resonance through space along a spiral trajectory. The signal can be sequentially refocused and acquired in an entirely spatiotemporal manner such that no Fourier Transform is needed for reconstruction. Because each resonance region can be treated entirely independently, this sequence has incredible potential for addressing problems that are inherently spatial in nature, such as B_1^+ and B_0 inhomogeneities.

Table of Contents

Table of Figures

Chapter 1: Introduction

Magnetic resonance imaging (MRI) is one of the most powerful and diverse tools available for clinical practice and research. MRI is an imaging modality with enormous potential to non-invasively give a wide variety of information about the body, such as anatomy, tissue micro-structure, chemical content, diffusion, metabolism, and blood flow. All of these uses of MRI are to varying degrees, limited by the need for increased signal-to-noise ratio (SNR) and spatial resolution, and these are the primary driving factors behind the current movement toward higher field strength MRI scanners. In addition to resolution gains, high fields bring the advantages of allowing increased image acquisition speed through better parallel imaging, as well as improved and novel types of contrast.

Body imaging at 7 T has become possible only very recently. The feasibility of doing clinically relevant scans at such high fields must be established, and the advantages of high fields for particular applications need to be explored. There are many obstacles to be faced in the advancement to 7 T. The main magnetic field (B_0) becomes less homogeneous in the body due to magnetic susceptibility effects. Also, the signal in the transverse plane (not aligned with the main magnetic field) decays more quickly, the rate of decay represented by the parameter T_2 (1). Moreover, constructive and destructive phase patterns due to the shortened wavelength are responsible for inhomogeneities in the radiofrequency (RF) transmit profile (B_1^+), risk of increased localized specific absorption ratio (SAR), and inefficiencies in transmit power.

This work first provides relevant and beneficial background information before presenting three novel research projects. An understanding of basic MR physics and imaging methods is fundamental for the entirety of this work. A general overview of the advantages, challenges, and methods for body imaging at 7 T will lay the foundation for the presentation of specific original work, and a closer look at the existing family of spatiotemporal sequences will facilitate the introduction of a novel pulse sequence as the newest member of that family.

A significant portion of this work is dedicated to establishing the feasibility of MR imaging and spectroscopy (MRS) of the liver and evaluating the advantages and disadvantages of 7 T imaging of the liver, with special attention given to parallel imaging. The inspiration to translate liver MRS up to 7 T was the increase of spectral dispersion with field strength. The evidence is compelling for the utility of MRS for cancer diagnosis and treatment monitoring. The liver is of particular spectroscopic interest because in addition to cancers originating in the liver, the liver is a common metastatic site for other types of cancer. The motion of the liver during breathing is a particular challenge but also an opportunity to take advantage of the increased parallel imaging performance available at high fields with highly parallel RF coils. The first demonstrations of liver imaging and spectroscopy are presented and evaluated.

Another large portion of the body of work presented here is the first demonstration of imaging of the uterus at 7 T with particular emphasis on contrast, which is especially important in distinguishing the layers of the uterus and the diagnosis and staging of benign and malignant legions. In establishing feasibility, clinically useful measurements

were conducted at 7 T, which was complemented by a comparison to a more commonly available field strength, specifically 3 T. An evaluation of relaxation rates at 7 T was conducted for both T_2 and T_1, the rate at which signal realigns with the main magnetic field. Further, the potential for measuring higher rotating frame relaxations such as adiabatic $T_{1\rho}$ and $T_{2\rho}$ independently or combined using the Relaxation Along a Fictitious Field (RAFF) method was evaluated. These novel contrast mechanisms are likely to be of particular value in imaging of the endometrium. The dynamic nature of the endometrium makes it a challenging and interesting target, not only for cancer, but also for better understanding infertility.

A common theme in both liver and uterus, and many other 7 T body applications, is the problem of inhomogeneous B_1^+. While B_1^+ shimming algorithms have been developed and improvements have been made, this often remains the most significant source of image degradation and may be the most significant obstacle currently facing 7 T body imaging in consistently producing clinical-quality images.

The largest portion of this work is the debut of a novel spatiotemporal pulse sequence for SWIRLY. This sequence employs a frequency and amplitude modulated excitation pulse in the presence of sinusoidal gradients to move a region of resonance through space along a spiral trajectory. The signal can be sequentially refocused and acquired in an entirely spatiotemporal manner such that no Fourier Transform is needed for reconstruction. Because each resonance region can be treated entirely independently, this sequence has incredible potential for addressing problems that are inherently spatial in nature, two prime examples being B_1^+ and B_0 inhomogeneities. Modulation of the amplitude and

frequency allow experimental compensation of field non-uniformities. The use of an inverse problem solution for the reconstruction of SWIRLY bestows it with additional capacity for retrospective compensation. Experimental results from SWIRLY imaging are shown, and Bloch simulations are used to demonstrate the use of SWIRLY for inhomogeneity compensation. SWIRLY can also be implemented in combination with SWIFT techniques for the acquisition of very short T_2 signals and the related benefits of SWIFT, opening opportunities to image many tissues previously thought to be outside the realm of MR, such as bone and lung. This sensitivity to short T_2 signals may also be of benefit in compensating for the shortening of T_2 at 7 T, making SWIRLY an even more beneficial sequence for high field imaging.

Finally, this work concludes with some discussion of the implications of the research presented. Consideration is given to future extensions and the development needed to achieve those objectives. Though 7 T body imaging and SWIRLY are not yet ready for clinical implementation, important applications are suggested for research pursuits.

Chapter 2: Fundamentals of Magnetic Resonance

2.1 Spins in a Magnetic Field

At the heart of MRI are magnetic fields and molecules with magnetic dipoles, particularly the behavior of these dipoles when perturbed while sitting in a magnetic field. Most molecules are magnetically neutral because the sum of the magnetic moments of their nuclear subatomic particles is zero. However, a few molecules remain magnetically unbalanced, including ^{13}C, ^{31}P, ^{17}O, ^{23}Na, and most useful and abundant ^{1}H. These molecular magnetic dipoles arise from nuclear magnetism as opposed to electronic magnetism, which is inherently much stronger since the dipole moment of an electron is stronger. Electronic magnetism can be used for electron spin spectroscopy (or electron paramagnetic resonance) in a manner somewhat analogous to the use of nuclear magnetism in nuclear magnetic resonance (NMR) spectroscopy. When placed in a magnetic field, the lowest energy state for any spinning magnetic moment is to align its z-axis component with the magnetic field, with parallel alignment, sometimes called spin up, being a slightly lower energy state than anti-parallel alignment, or spin down. Consequently there will be a slight majority of dipoles aligned parallel to the field. This relationship can be written as

$$\frac{N_{down}}{N_{up}} = e^{\frac{-\Delta E}{kT^\circ}} \qquad (1)$$

where N_{down} and N_{up} are the number of dipoles in the spin down and spin up positions respectively, ΔE is the energetic difference between the up and down positions, k is

Boltzmann's constant (k = 1.381 x 10^{-23} J/K) and T° is temperature. The difference between the spin up and spin down energy states is dependent on the strength of the magnetic field (B_0) and the gyromagnetic ratio of the nucleus (γ), shown by the following relationship

$$\Delta E = h\gamma B_0 \tag{2}$$

where h is Planck's constant (h=6.626 x 10^{-34} Js). An additional result of placing a spin in a magnetic field arises from the nucleus's inherent constant angular momentum which will cause the dipole to gyroscopically precess about the magnetic field at a rate known as the Larmor frequency given as follows

$$\omega_0 = \gamma B_0 \tag{3}$$

When spins are perfectly aligned with the magnetic field at equilibrium this precession is non-existent. The importance of the precession arises when the spins are forced from their equilibrium alignment by an addition of energy to the system, which will be addressed shortly.

From a classical mechanical standpoint, this relationship between magnetic field and the sample magnetization can be described as

$$\frac{d\mathbf{M}}{dt} = \gamma \mathbf{M} x \mathbf{B_0} \tag{4}$$

where t is time, **M** is a vector describing the net magnetization of an ensemble of spins sharing a Larmor frequency, or isochromat, and $\mathbf{B_0}$ is the vector describing the magnetic field which is most often generated by a super-conducting solenoid (2). Expanding the mechanical description given in equation (4) into vector components

$$\begin{aligned}\frac{dM_x}{dt} &= \gamma(B_z M_y - B_y M_z)\\ \frac{dM_y}{dt} &= \gamma(B_x M_z - B_z M_x)\\ \frac{dM_z}{dt} &= \gamma(B_y M_x - B_x M_y)\end{aligned} \tag{5}$$

Typical assignment of Cartesian coordinates in MRI sets the z-axis along $\mathbf{B_0}$, which is often called the main magnetic field, and refers to the plane defined by the x- and y-axes as the transverse plane. $\mathbf{B_0}$ might be though of as having magnitude B_0 with Cartesian direction (0,0,1). The resulting Bloch equations are

$$\begin{aligned}\frac{dM_x}{dt} &= \gamma B_0 M_y\\ \frac{dM_y}{dt} &= -\gamma B_0 M_x\\ \frac{dM_z}{dt} &= 0\end{aligned} \tag{6}$$

combining with equation (3) to give the solutions

$$\begin{aligned}M'_x(t) &= M_x \cos(\omega_0 t) - M_y \sin(\omega_0 t)\\ M'_y(t) &= M_y \cos(\omega_0 t) + M_x \sin(\omega_0 t)\\ M'_z(t) &= M_z\end{aligned} \tag{7}$$

Notice the time dependence. These solutions are given with respect to the laboratory frame, as opposed to the rotating frame which will be introduced later.

In addition to the super-conducting solenoid, there are often three sets of gradient coils, one per Cartesian direction, that are used to apply a spatially varying magnetic field that is temporary and small compared to the main magnetic field. Because the field is spatially variant, isochromats in different locations experiencing different magnetic fields

will then precess at different frequencies. In essence the different locations are assigned different addresses by their frequency so that spins at different locations can be distinguished and spatial information resolved. The effects a gradient applied along the z-axis can be incorporated into equation (3) above as follows

$$\omega = \gamma(B_0 + G_z z) \tag{8}$$

In addition to the main gradient coils there are also shim coils (3). These are used to make minor adjustments to the magnetic field in order to maximize the homogeneity.

2.2 Perturbation and Relaxation

In a MR experiment radio frequency (RF) coils are used much like radio antennas and within the same frequency range, hence the name. These coils can be tuned to resonate at the Larmor frequency. The current in the coils induces a magnetic field, transmitting energy to the system and perturbing the spins at the Larmor frequency from their equilibrium alignment with the main magnetic field into the transverse plane. This RF magnetic field is described by the vector $\mathbf{B_1}$. This can be introduced into the Bloch equations to produce the vector components

$$\begin{aligned}
\frac{dM_x}{dt} &= \gamma M_y B_0 + M_z \gamma B_1 \sin(\omega_1 t) \\
\frac{dM_y}{dt} &= M_z \gamma B_1 \cos(\omega_1 t) - M_x \gamma B_0 \\
\frac{dM_z}{dt} &= M_x \gamma B_1 \sin(\omega_1 t) - M_y \gamma B_1 \cos(\omega_1 t)
\end{aligned} \tag{9}$$

Having been rotated partially or entirely into the transverse plane by the RF field, the spins will precess about the main magnetic field. These precessing spins will generate a time-varying flux, which induces a voltage in the RF coil. The signal received by the coil is amplified, demodulated, converted from analog to digital, and filtered (4).

With the RF magnetic field removed, the spins then return to the lower energy state of alignment with the main magnetic field. The rate at which they return is captured in the time constant T_1. Another important time constant is T_2, which describes the rate at which the signal in the transverse plane decays (1). In addition to the intrinsic decay, there may also be decay arising from B_0 inhomogeneities referred to as T_2', which may be able to be recovered unlike the intrinsic T_2. The sum of these is often a useful term called T_2*. Adding these relaxation effects to the set of equations above and converting to Cartesian coordinates we get the Bloch equations (2,5,6)

$$\begin{aligned}
\frac{dM_x}{dt} &= M_y\gamma B_0 - M_z\gamma B_1 \sin(\omega_1 t + \phi) - \frac{M_x}{T_2} \\
\frac{dM_y}{dt} &= M_z\gamma B_1 \cos(\omega_1 t + \phi) - M_x\gamma B_0 - \frac{M_y}{T_2} \\
\frac{dM_z}{dt} &= M_x\gamma B_1 \sin(\omega_1 t + \phi) - M_y\gamma B_0 \cos(\omega_1 t + \phi) - \frac{(M_z - M_0)}{T_1}
\end{aligned} \tag{10}$$

One useful way of discussing spins precessing at the Larmor frequency is to consider them in a rotating frame such that any spin rotating about the main magnetic field at the Larmor frequency appears stationary; the frame in which they do appear to rotate is called the laboratory frame (7). A prime symbol can be used to indicate the rotating frame axis (x',y'), though dropping the primes and assuming the rotating frame is in view is not uncommon, as will be done here.

2.3 Acquisition and Assignment

Frequency encoding

The simplest means of acquiring MR signal is to apply a RF pulse to tip the spins into the transverse plane and then collect the signal as it decays. The form of the signal is called free induction decay (FID). However, without any gradients the signal from various locations cannot be distinguished. If a spatially varying gradient is applied following the RF pulse this will cause the spins to precess about the main magnetic field with different frequencies, as discussed earlier. Accordingly, the various isochromats will induce voltage in the coil corresponding to the frequency at which they are precessing (8). The amplitude of the contribution from each frequency will correspond to the number of spins that are at that position, which is called the spin density. In biological systems the abundance of water means that the signal will typically be dominated by the contribution of the hydrogen protons, so spin density can largely be thought of as interchangeable with proton density or water content. The FID will be a combination of all of the frequencies, which can be separated through the use of a Fourier transform (FT). Having extracted the contribution of each frequency to the FID and knowing the spatial variation induced by the gradient, the signals can be assigned to their location according to their frequency address. This means of assigning signal is called frequency encoding.

Phase encoding

Phase encoding, like frequency encoding, requires the application of a spatially varying gradient following a RF excitation pulse. The amount of phase that an isochromat

accumulates is proportional to the product of the gradient strength and the length of time it is applied (9). When repeated with incremental time or gradient strength, the signal associated with various phases can be mapped and the signal assigned spatially. Generally the time domain, or *k*-space, is filled by acquiring one line of frequency encoding for each increment of the phase encoding.

Slice selection

With the capacity to cover two dimensions with frequency and phase encoding, slice selection is often the means of spatially distinguishing signal in the third dimension (9). Again, a gradient pulse is applied in so as to produce a variation across the dimension of interest. In the case of slice selection, the gradient is applied during the RF pulse. Only the spins that are within the bandwidth of the excitation pulse will be rotated into the transverse plane. Only the spins in the transverse plane will contribute to the acquired signal.

Time encoding

Time encoding can be traced back to a very early means of acquiring nuclear magnetic resonance (NMR) spectra. In it's early form this method was called continuous wave. Continuous wave spectroscopy was most commonly acquired by keeping the frequency constant and sweeping the magnitude of B_0 or by keeping the B_0 magnitude constant and sweeping the frequency, the latter being more akin to current time-encoding methods. With the addition of a gradient to spatially vary the frequency, continuous wave imaging

could be performed, sweeping across the range of frequencies. Temporal information could be converted to spatial information as the isochromats at each spatially-dependant frequency were excited only when their frequency corresponded to that of the temporally-dependant RF frequency. While not a time-encoded sequence, SWIFT is a modern example of a sequence that employs a continuous wave. In more recent years time encoding has emerged as a means for producing multi-dimensional images and spectra in a single scan for ultra-fast imaging and spectroscopy (10-21). These sequences will be presented in greater detail in Chapter 4.

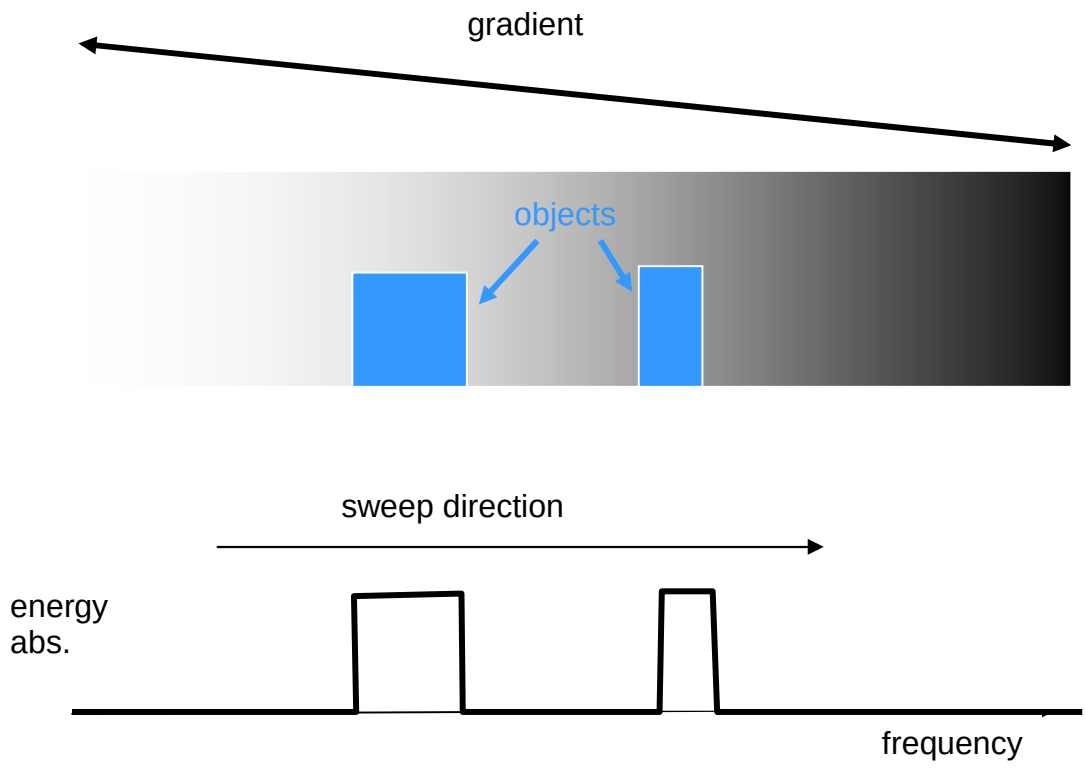

Figure 2.1 - Continuous wave imaging in one dimension

2.4 Imaging

Gradient echo

One common type of pulse sequence used for imaging is the gradient echo (GRE). Gradient echo sequences are fast and thus generally employed for applications requiring rapid acquisitions. In GRE sequences a small tip angle can be used which reduces the time needed for T_1 recovery and produces sufficient signal in the transverse plane while losing little of the longitudinal magnetization. Consequently the total time before the sequence can be repeated, or TR, can be short. The repetition time (TR) is the spacing between the center of the first pulse and the center of the last pulse. The echo time (TE) is measured from the center of the excitation pulse to the center of the acquisition. In a basic GRE sequence, an RF pulse is applied to tip the spins away from the main magnetic field. Concurrently a gradient is turned on in the direction desired for slice selection. The excitation and slice selection are followed by phase encoding. Finally signal is acquired in the presence of a frequency-encoding gradient. The signal will be in the form of an echo.

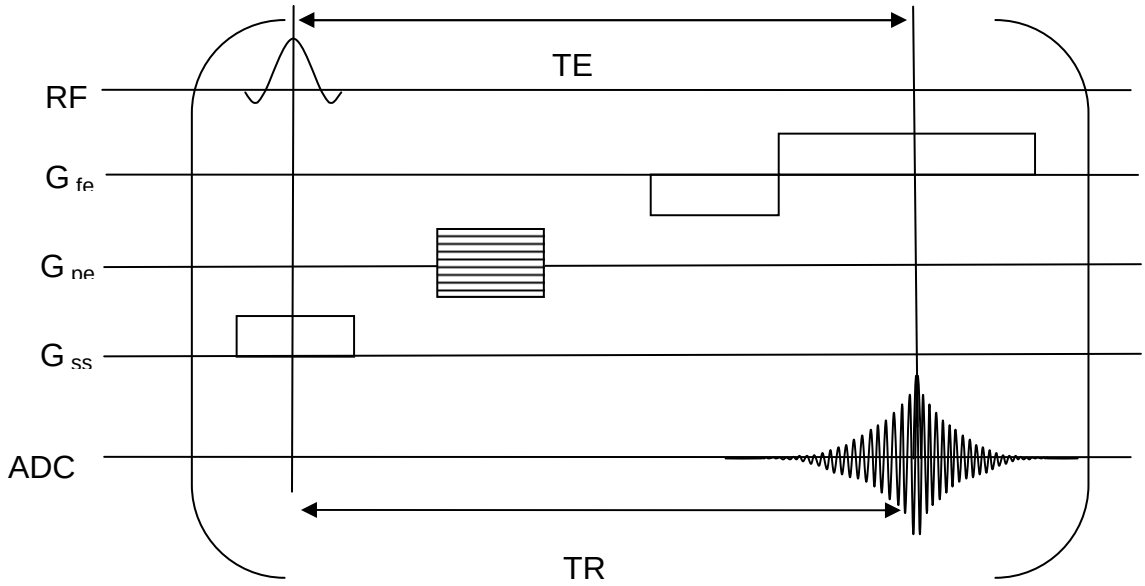

Figure 2.2 - Gradient echo sequence

Spin echo

Another basic and widely used form of pulse sequence is the spin echo (SE). The primary advantage of spin echo imaging is its ability to provide various kinds of contrast by adjusting the TR and TE, or time between the excitation and acquisition. Using short TR and TE produces T_1 weighting. Using long TR and TE produces T_2 weighting, and using long TR and short TE produces proton density weighted imaging. Spin echo also has the advantages of being more robust in the presence of off-resonance effects. In a basic spin echo the excitation pulse rotates the spins 90° from the main magnetic field into the transverse plane. Once in the transverse plane a frequency-encoding gradient is applied and the spins will begin to dephase. In the presence of the gradient some will dephase more quickly than others. A phase-encoding gradient may be applied before or after the

inversion. An inversion RF pulse is applied which flips the transverse plane 180°. Another gradient is applied in the frequency encoding direction which reverses the direction of the dephasing so that all of the spins come back into phase simultaneously as the gradient experienced after the inversion pulse balances the gradient experienced before the pulse. This refocusing forms an echo. Slice selection is often applied during both excitation and inversion.

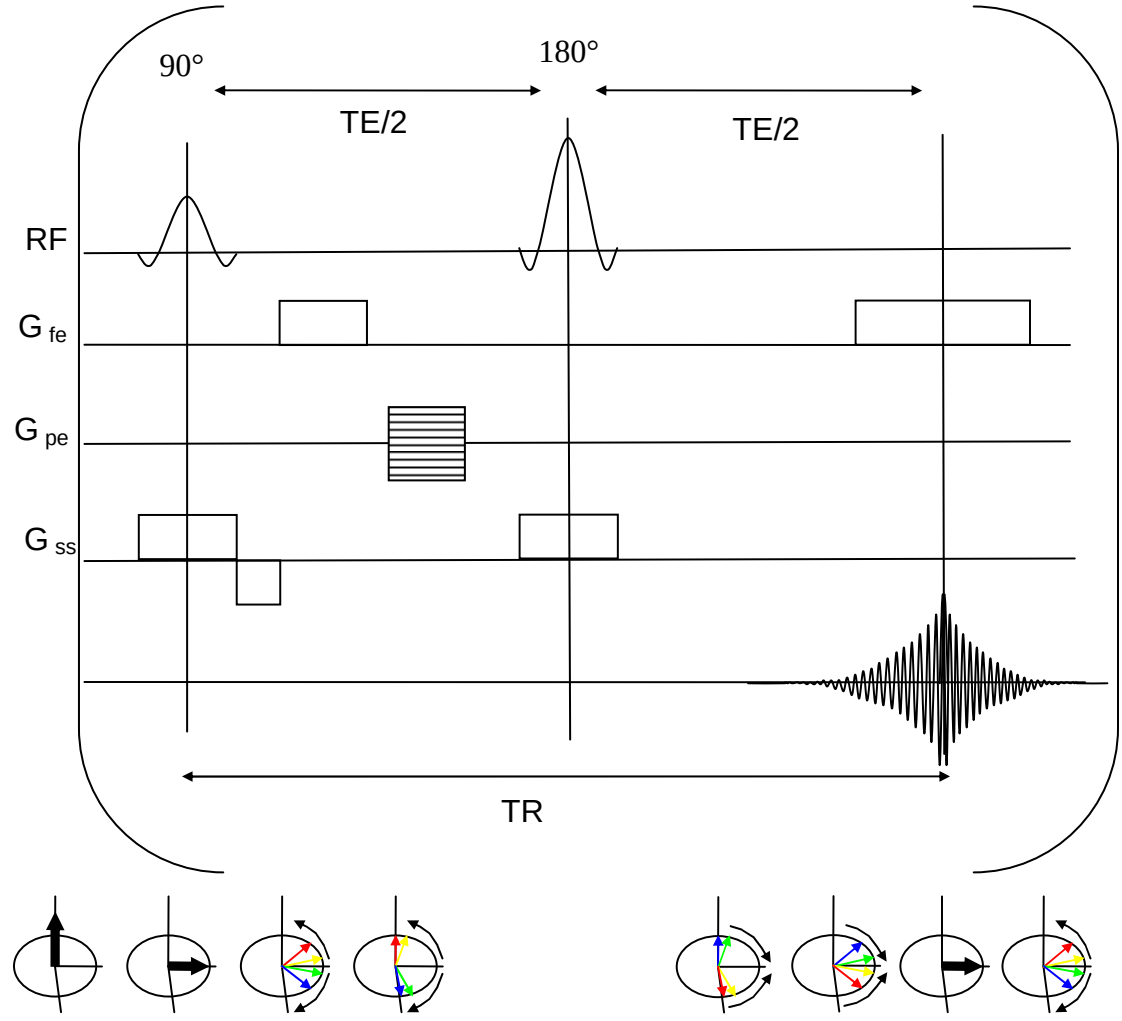

Figure 2.3 - Spin echo sequence. The series of diagrams below shows the dephasing and rephrasing of the signal.

Chapter 3: High Field Body Imaging

3.1 Introduction

In the pursuit of better imaging and spectroscopy, increasingly higher field strengths have been sought by researchers. With each field strength increase the feasibility must be demonstrated and the advantages shown. To do this, hardware must be adapted, optimal parameters determined, protocols developed, and new challenges discovered and addressed (22-24). Much hard work is required to stabilize and standardize these systems to function in a clinical setting, but the ever-increasing number of 3 T systems in hospitals is evidence that demand is rising. The new frontiers of higher fields await discovery.

While brain imaging at 7 T is becoming more widely used as a research tool, though not yet approved for clinical applications, body imaging at that field is only now being explored (25). Because the wavelength (λ) of a proton NMR signal at 7 T is smaller than the diameter of a human, obtaining a uniform B_1^+ RF transmit field within the body is a substantial challenge (26). Furthermore, with shorter wavelengths the SAR (specific absorption ratio) becomes more difficult to keep within an acceptable range. Additionally, B_0 homogeneity decreases. Despite these challenges great potential is being realized not only in the increased signal to noise (24) but also in parallel imaging performance (27,28) and novel or improved contrast mechanisms (29-36).

3.2 Effects of Increased B_0

There are many consequences of moving to higher B_0 systems. Increased SNR is of course of primary interest, which is approximately linear with field strength. However, a comparison of 4 T to 7 T showed that while the average SNR increases linearly, the increase is not spatially uniform (24). Another benefit is spectral dispersion. One of the drawbacks is increased B_0 inhomogeneity because of the increased sensitivity to susceptibility artifacts, which actually becomes an advantage if susceptibility contrast is the objective as with BOLD (blood oxygen level dependant) contrast for fMRI (functional magnetic resonance imaging). The increased B_0 also causes increased resonant frequencies and shorter RF wavelengths. The resonant frequency of ^1H at 7 T is 300 MHz, the beginning of the ultrahigh field range, which corresponds to a wavelength of approximately 12 cm in tissue. Such short wavelengths relative to the size of the object of interest, in this case a human torso, can produce wave-like behavior in the RF fields. This wave-like behavior will result in constructive and destructive interference. Accordingly there will be regions of the object that will experience high RF, which causes concern about RF deposition and tissue heating, particularly from the electrical fields, and there will be regions that experience very little RF and consequently cause low-signal regions in the images, which is dependent on the magnetic fields rather than the electrical.

3.3 Hardware

In most clinical systems, images are acquired with separated transmit and receive coils. Transmit is performed by a large cylindrical coil that is approximately homogeneous and is tuned to excite a wide band of frequencies. Receive may be performed with the volume coil but is often done with local receive coils placed close to the region of the body that is of interest to maximize signal detection efficiency. Using such large volume transmit coils at high fields is substantially more challenging. The birdcage design widely used in clinical scanners is inherently ill suited for high-field applications because large circumscribing, single channel volume coils, such as birdcage coils, are inefficient at higher frequencies because the electrical length of the circuit is significantly greater then 0.1λ, which drastically increases the radiative losses of the coil. Work is in progress to produce a stable, efficient single-channel transverse electromagnetic (TEM) volume coil for high fields, but with the formidable hurdles from SAR and B_1 inhomogeneities, implementation remains challenging (37,38). Consequently, for high fields multi-channel arrays of TEM/stripline coils for both transmit and receive have been important components of high field advances (39,40). The flexibility to control individual channels in a multi-channel array is particularly advantageous in efforts to compensate for RF interference patterns (26,36,40-42). Using multiple channels is also important for parallel imaging. The RF transmission profile, or B_1^+, needs to be homogenous over the region of interest in order to produce high quality images, where as inhomogeneities in the RF receive profile, or B_1^-, can benefit images through improved parallel imaging performance (27,43). Accordingly, there has been a general trend toward higher numbers

of channels for greater acceleration (44). There is ultimately a limit to how much can be gained from additional channels as individual coil elements must be large enough to obtain adequate RF penetration and yet arranged over the region of interest with sufficiently distinct RF profiles (44). Another immediate limitation on the number of coil elements is the need for individual phase and gain controlled amplifiers for each channel for B_1^+ inhomogeneity compensation. This limit may be somewhat sidestepped by increasing the number of channels on the receive side for higher parallel imaging performance but without gain for B_1^+ inhomogeneity compensation (38).

3.4 B_1^+ Inhomogeneity

B_1^+ inhomogeneity is arguably the greatest challenge facing 7 T body imaging. Several strategies have been developed to address this issue. One approach is through static B_1^+ shimming (26,36,41,45). Static B_1^+ shimming requires mapping the transmit profile of each of the RF channels. Then a region of interest is specified. This information can be used with an algorithm designed to calculate the optimum combination of phases to minimize the destructive interference over the specified region. Another method for B_1^+ inhomogeneity compensation is to exploit the complementary RF patterns created by exciting in different modes (42,46,47). Time Interleaved Acquisition of Modes (TIAMO) uses B_1 maps to generate two sets of amplitudes and phases, which are designed to be complementary such that the regions of interference do not overlap between the two modes. These modes are applied alternately during imaging. The interleaved modes can be combined to form a more homogenous image.

3.5 Parallel Imaging

The complexity of the B_1^+ transmit profile is complemented by the complexity of the B_1^- RF receive profile which makes parallel imaging particularly powerful at high magnetic field strengths (43). The differing receive sensitivities of the coils in a multi-channel system can be used to great advantage. The wave-like behavior of RF at increasingly high field strengths results in increasingly distinct RF sensitivity profiles. When the sensitivity profiles are combined into one matrix, the distinctness of the profiles will directly correlate to the degree to which the complex conjugate transpose is well conditioned. A well conditioned solution will minimize the noise amplification that occurs when that solution is used to unfold an image for which *k*-space has been under sampled. Conditioning is generally described by a *g* factor (geometry factor). Lower *g* factors correlate to higher SNR.

3.6 Recent Progress

Much progress has recently been seen in body imaging at 7 T. Both imaging and spectroscopy have been demonstrated in the breast and prostate (25,26). The prostate's size, shape, and location make it a good candidate for demonstrating the benefits of B_1^+ shimming. The improvements shown with the use of B_1^+ shimming are very promising, increased transmit efficiency, lower RF power requirements and consequent reduced SAR, and of course uniform B_1 over the region of interest, producing high quality images (26). Additionally 7 T cardiac imaging has been successfully shown (48). Further work has demonstrated the feasibility of performing coronary angiography (49) and using

FLASH cine and SSFP to produce quality cardiac images at 7 T (50-52). Other presentation of successful 7 T body imaging include liver (53-55), uterus (56,57), and kidneys (58).

Chapter 4: Spatiotemporal-Encoded Sequences

4.1 Introduction

For the majority of MR imaging, data is acquired using frequency encoding, phase encoding, or a combination of both often in conjunction with slice selection. Another encoding dimension is spatiotemporal encoding, often referred to as either spatial encoding or temporal encoding, the variable nomenclature arising from the linear relationship between time and space imparted by the use of a chirped pulse, an RF pulse with a constant amplitude and frequency swept at a constant rate, along one dimension such that time and space are linearly related. Thus it is acceptable to use temporal encoding, spatial encoding, and spatiotemporal encoding interchangeably.

4.2 Encoding in phase and time: The Frydman Group

In one variety of spatiotemporal imaging the frequency encoding is replaced with time encoding (12,13,16,19,21). Consider a simple 1D experiment. The application of a gradient along that axis will impart a spatially-dependant range of frequencies. If an RF excitation pulse with a chirped frequency sweep is applied concurrently, as the RF frequency is swept, the isochromats at each frequency will be perturbed into the transverse plane sequentially. The phase of each isochromat will be a combination of the phase acquired from the RF excitation and the phase accumulated while freely precessing after having been tipped into the transverse plane. By applying a gradient in the opposite direction the phase of each isochromat can be unwound, beginning with the last to be

excited and proceeding in a spatially sequential manner back to the isochromat that was excited first. As each isochromat is unwound an FID will be generated. The signal can then be assigned to the corresponding spatial location (12,13,16,19,21).

To expand to 2D, a phase encoding direction may be added. One implementation is to acquire time encodes between phase steps. After traversing the time encoding direction, step the phase, and then reverse the time encoding gradient again to traverse the time encoding dimension and repeat for the desired number of phase steps. Alternating lines of spatial encoding in the hybrid *k*-space will need to be reversed before a 1D FT can be applied along the phase axis. Alternatively, after the chirped RF pulse a line of phase may be collected followed by a small gradient in the opposite direction as applied during excitation to unwind the next set of spins in the spatial dimension. The phase acquisitions and spatial encoding steps can be repeated until the spins at each spatial position have been addressed. For this version the alternating lines of phase in the hybrid *k*-space will need to be flipped before the application of the 1D FT (12,13,16,19,21).

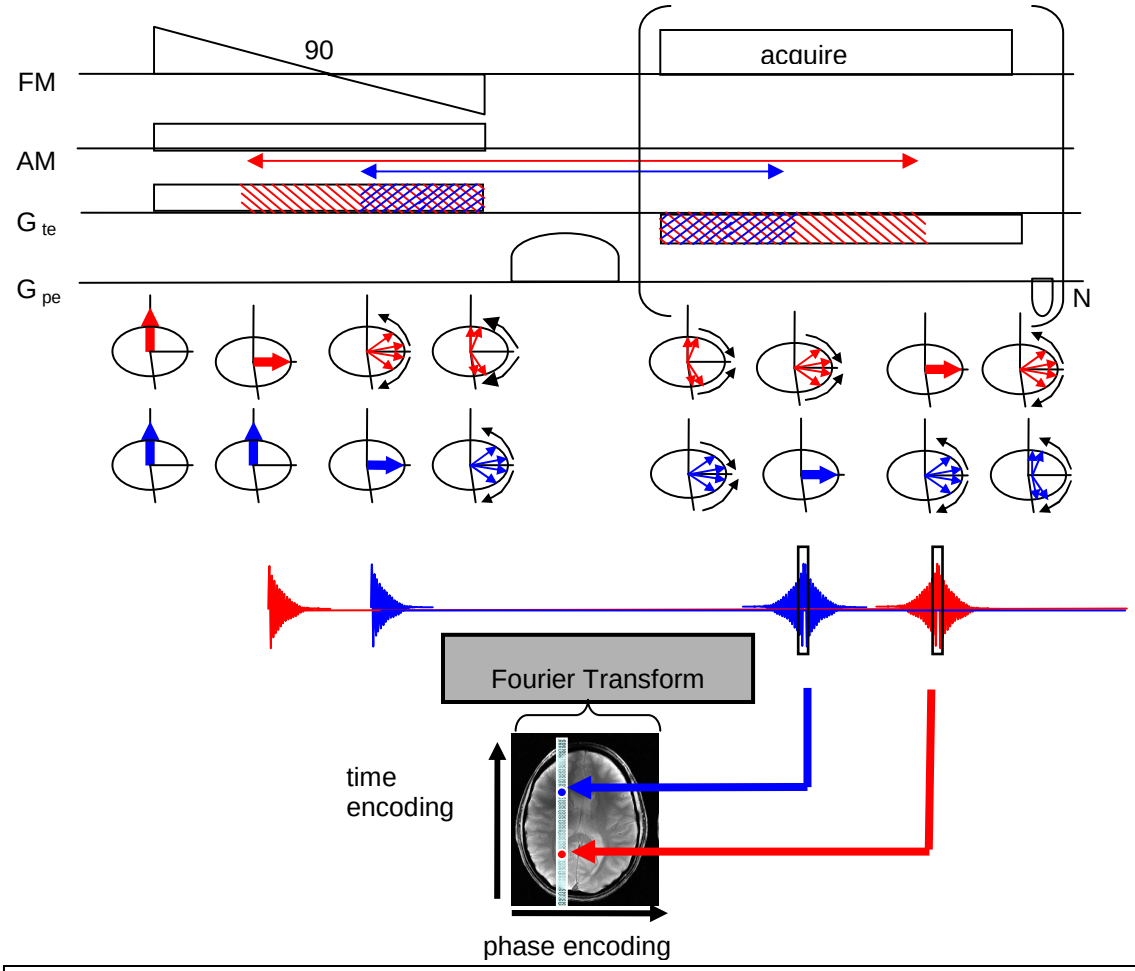

Figure 4.1 – Encoding in phase and time, as employed by the Frydman group. The pulse sequence diagram is on top. The upper and lower spin diagrams represent two different points along the object. The spin behavior and signal pattern are below as well as correlated spatial position.

4.3 Encoding in frequency and time: RASER

Spatiotemporal encoding can also be used as a replacement for phase encoding (10). This is the means by which Rapid Acquisition by Sequential Excitation and Refocusing (RASER) works. As with the previously discussed time-encoding sequence, a chirp pulse is applied in combination with a gradient along the intended time encoding direction

causing a spatially dependent accumulation of phase. An inversion pulse, specifically an adiabatic inversion pulse, is applied, generally coupled with a slice selective gradient. The sequential unwinding or dephasing of the spins can be accomplished with a gradient like the first. The last spins to be excited will now be the first to be rephrased. After each isochromat is rephrased it will then continue to acquire phase, being wound in the opposite direction. A second adiabatic inversion pulse (and slice selective gradient) are applied. Any phase effects from the first adiabatic pulse will be canceled. Acquisition begins as another gradient like the first two will now unwind the phase that was accumulated by each spin after the previous rephasing. The isochromats will now rephase in the same order that they were originally tipped into the transverse plane, which means that the echo time (TE) will be the same across the time-encoded dimension. During the acquisition a frequency-encoding gradient is applied in an alternating manner. An echo is collected for each frequency encoding alternation. This series of echos can cover a hybrid *k*-space, filling frequency-encoding lines as each portion of the spatiotemporal encoding direction is refocused. Every other frequency encoding line will be reversed before the 1D FT is applied. The third gradient can be applied either continuously or as a series of short pulses ultimately that sum to the same area under the gradient as the continuous version. In the case of the series of short pulses, these pulses fall between each traversal of the frequency-encoding dimension filling in the spatiotemporal-encoding dimension in a step-wise manner. The continuous third gradient version will require minor adjustments to account for the spatiotemporal change across each frequency-encoded line (10).

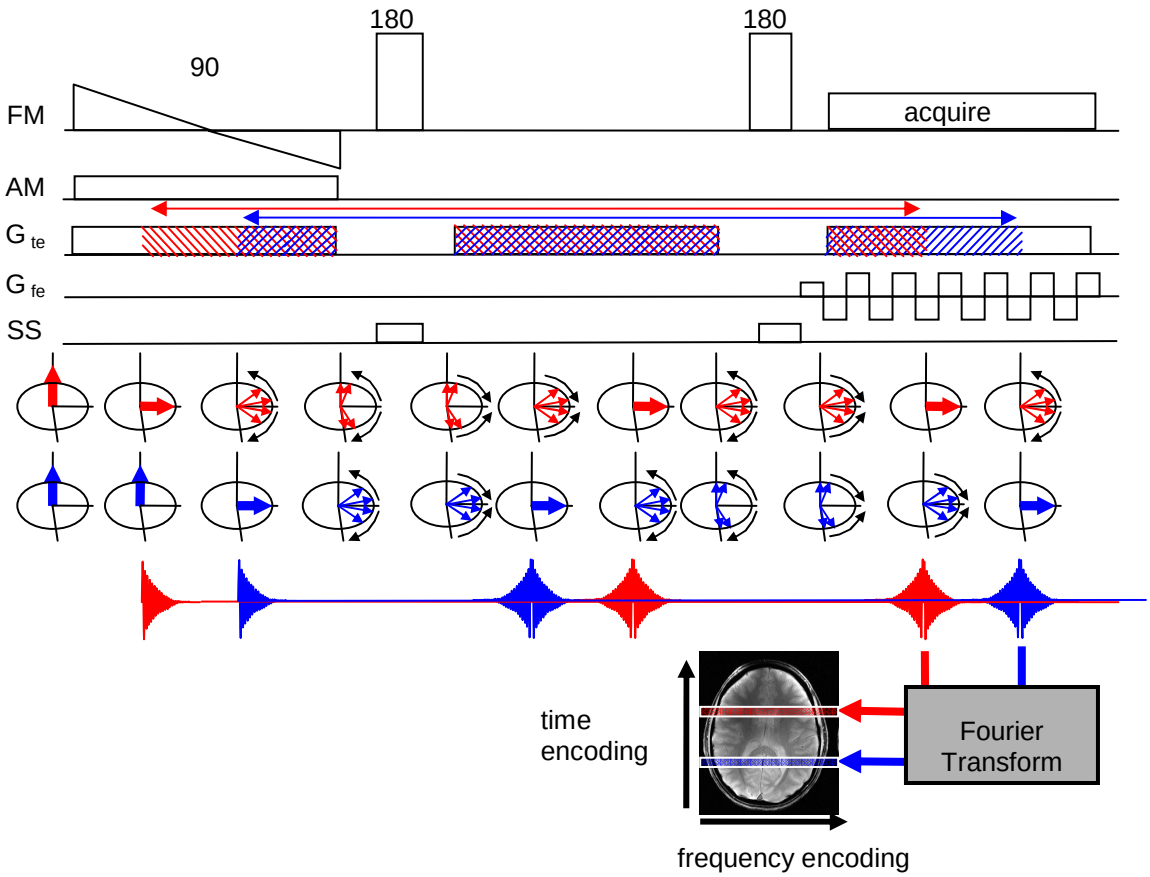

Figure 4.2 – RASER, used for encoding in frequency and time. The pulse sequence diagram is on top. The upper and lower spin diagrams represent two different points along the object. The spin behavior and signal pattern are below as well as correlated spatial position.

4.4 Advantages over EPI

EPI sequences can acquire a 2D slice in a single shot making for very fast imaging times. However, they suffer from numerous artifacts. The long acquisition time of EPI makes it prone to susceptibility artifacts. Like EPI the two sequences presented above can also acquire images very quickly in a single shot, only they substitute one of the traditional *k*-

space dimensions with time encoding. As a result, only one line or slice is in phase at any given time, reducing artifacts from tissue interfaces, inhomogeneous fields, and chemical shift (10,12,13,16,19,21). Moreover, B_1 and B_0 inhomogeneities that degrade EPI images can be better compensated for with spatiotemporal sequences (12,13,16,19,21). Many of the imaging artifacts that plague EPI are alleviated with these spatiotemporal methods suggesting a valuable role for spatiotemporal encoding for fMRI and other rapid acquisition experiments.

Chapter 5: MRI and MRS of the Liver at 7 T

Significant contributions to this work were made by Patrick J. Bolan.

Ultra-high magnetic fields have the potential to improve the quality of MRI and MRS by giving increased SNR, better image contrast, and increased spectral dispersion. Further advantages are gained in high fields by capitalizing on the increased parallel imaging performance. Body imaging at 7 tesla is feasible but challenging due to B_0 inhomogeneity, B_1 inhomogenetiy, and SAR limitations. Presented here are the first data showing the feasibility of *in vivo* liver MRI and MRS at 7 T and explore the potential of parallel imaging at 7 T for particular application to liver imaging.

5.1 Introduction

MRI can be used to diagnose diseases of the liver including cirrhosis, hepatocellular carcinoma, and metastatic liver disease (59). MRI and MRS can play an important role in treatment-response monitoring for cancers, including tumors originating in the liver as well as metastatic tumors in the liver with remote primary locations locations (60). One of the major challenges of liver imaging is dealing with motion from breathing. A common solution is to acquire images during a breath-hold. However, patient health and compliance limit the feasible breath-hold duration. Trained breathing and respiratory-gated imaging are also possible ways to deal with respiratory motion, but the former requires a high degree of patient compliance, and the latter is not compatible with all sequences.

Ultrahigh magnetic fields have the potential to improve the quality of MRI by giving increased SNR. Additionally, spectral dispersion of high fields can improve the precision of quantitative MRS and allow detection of metabolites not visible or poorly resolved at lower field strengths (61). With these gains come the challenges of increased B_1^+ and B_0 inhomogeneity. Generating a uniform B_1^+ field across the entire liver with a multi-channel transmit systems is challenging. Advancements have been made for generating a homogeneous RF transmit field over smaller regions of interest, but more development is needed for the large FOV necessary for the liver (26,45). However, the increased B_1^- field can be advantageous in parallel imaging, as the increased B_1^- inhomogeneity lowers the g-factor (27,43). The reduced g-factors at high field facilitate both higher temporal and spatial resolution without additional time, which is very useful in liver imaging for compensating for breath-hold limitations. Dynamic contrast enhancement (DCE) liver imaging is typically performed with a single baseline and two post-contrast time points. By shortening the time required to collect images, more post-contrast images can be acquired, increasing the amount of dynamic information and aiding in pharmacokinetic modeling, making parallel imaging at 7 T a valuable tool for understanding normal and abnormal vasculature.

5.2 Imaging

Methods

Healthy volunteers were studied under a protocol approved by our institution's IRB. MRI and MRS of the liver were collected on a research system with a 7 T magnet (Magnex Scientific, Oxfordshire, UK), with a Siemens Sonata gradient system and TIM console (Siemens, Erlangen, Germany). A novel, 8- or 16-channel flexible body surface array with TEM/stripline elements was used to both transmit and receive (44). With the 8-channel coil, the transmit signal from an 8-kW RF amplifier (Communications Power Corporation, Hauppauge, NY) was split with equal phase and gain by an 8-way power divider and phase-modulated using variable cable lengths and high-power phase shifters (Advanced Technical Materials, Patchogue, NY) for each transmit element. With the 16-channel coil, each element was driven by an individual 1-kW RF amplifier with independent phase and gain control (Communications Power Corporation, Hauppauge, NY). The transmit power envelope was monitored in real-time on all transmit channels using an in-house built 16-channel RF monitoring system. In both cases, the transmit phase for each of the channels was optimized *in vivo* using a B_1 shimming algorithm (26,45). Figure 5.1 shows the distribution of the elements of the 16-channel coil and the respective RF transmit profile for each channel. The transmit sensitivities were used to determine the optimal phase values for each channel to minimize destructive interference in the region of interest. Images from the 8- and 16-channel coils are shown in Figure 5.2. The images are from two different subjects; a rigorous comparison is not intended.

However the images effectively show greater homogeneity with the increased number of channels. (For a more thorough comparison, see reference (44).)

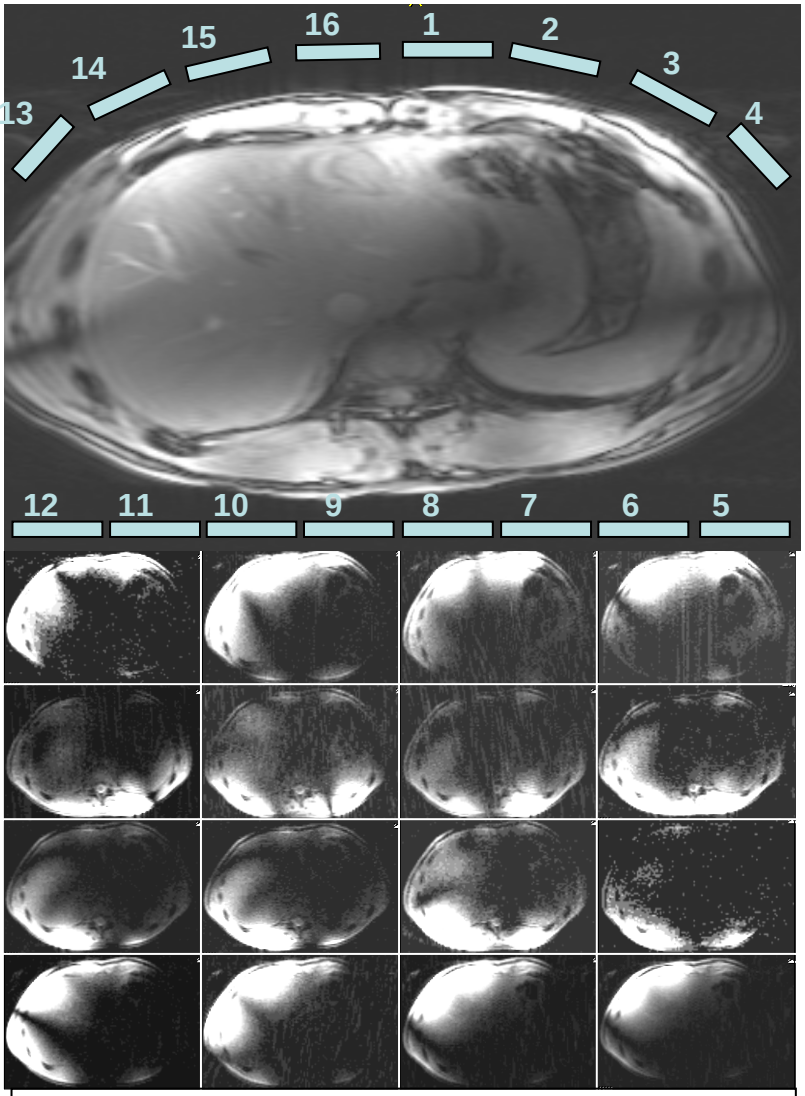

Figure 5.1 - 16-channel body coil and the placement and sensitivity of each element

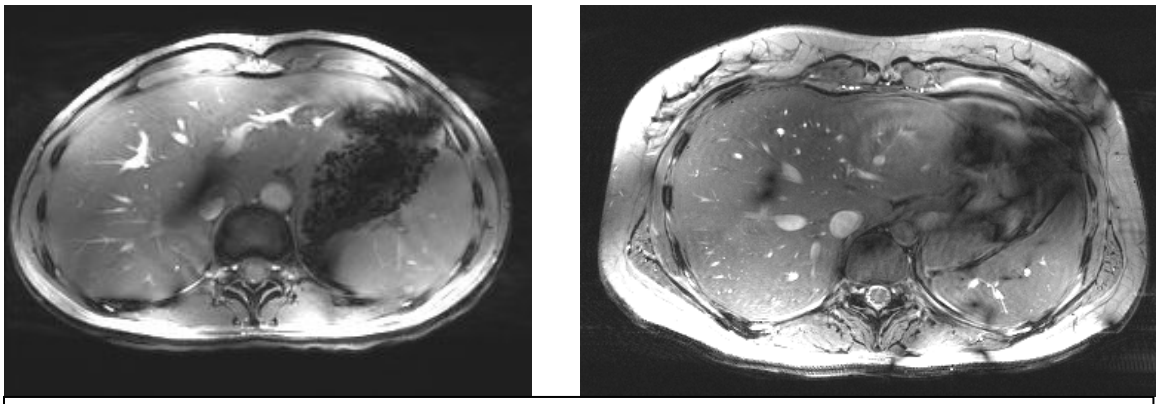

Figure 5.2 – GRE images acquired using 8-channel (left) and 16-channel (right) coils

Prior to imaging, the B_0 inhomogeneity was minimized using the manufacturer's 3D phase map algorithm, and the B_1 shimming was performed over an approximately 5 x 5 cm region in the anterior of the right lobe of the liver. Multichannel image reconstruction was performed using the manufacturer's root-sum-of-squares algorithm. For each subject, multi-slice gradient recalled echo (GRE) images and GRE images with variable flip angles (GRE-VFL) were acquired during brief breath-holds. Figure 5.3 shows a representative image from a multi-slice GRE acquisition (eight 5 mm slices, TR =150 ms, TE = 4 ms, FOV = 26 cm, 256 x 256 matrix, 66 kHz readout bandwidth) acquired over two 20s breath-holds and a GRE-VFL image (one 5 mm slice, TR = 100 ms, TE = 10 ms, FOV = 26 cm, 256 x 256 matrix) acquired in one breath-hold.

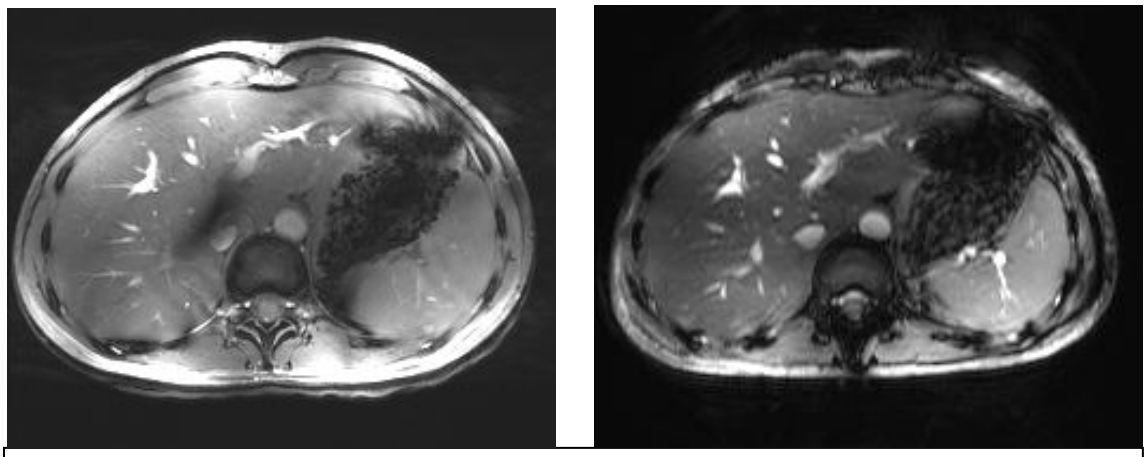

Figure 5.3 – An axial image from a multi-slice gradient recalled echo image acquired over two 20 s breath-holds (left) and an axial image using a gradient recalled echo, variable flip angle sequence in one breath-hold (right)

Results

The gradient-echo images generally have good SNR but show some remaining inhomogeneity. They can be successfully acquired during breath-holds or with triggering using respiratory bellows. Figure 5.4 shows six slices from a multi-slice GRE with TR = 75 ms, TE = 4.0 ms, and 1.4 x 1.4 x 3.0 mm resolution. These images were collected during a 20 s breath-hold. Some destructive interference is visible in the upper right portion of the image. Also, a flow artifact from the aorta can be seen in the liver anterior to the aorta. The B_1 shimming algorithm greatly improved the homogeneity of the images, removing a majority of the destructive interference in the region of interest. A few areas of interference remain in the images as the algorithm used here was developed primarily for smaller regions. Further improvements would be required to make the images of diagnostic quality.

Images were collected with fat and water in and out of phase, which is a clinically

important scan for the diagnosis of fatty liver disease (Figure 5.5). On top are two GRE 2D multi-slice images, the left one in-phase, TE = 3.06 ms, and the right out-of-phase, TE = 4.57 ms. Below on the left are zoomed versions of the upper images to better show the constructive and destructive interference at the fat-water boundary (as indicated by the arrows).

Collection of T_2-weighted images is still far from optimal. In the lower right-hand corner of Figure 5.5 is a HASTE (Half-Fourier acquired single-shot turbo spin echo) image with TE = 152 ms. Artifacts are evident in the fat, and liver structure is somewhat difficult to detect.

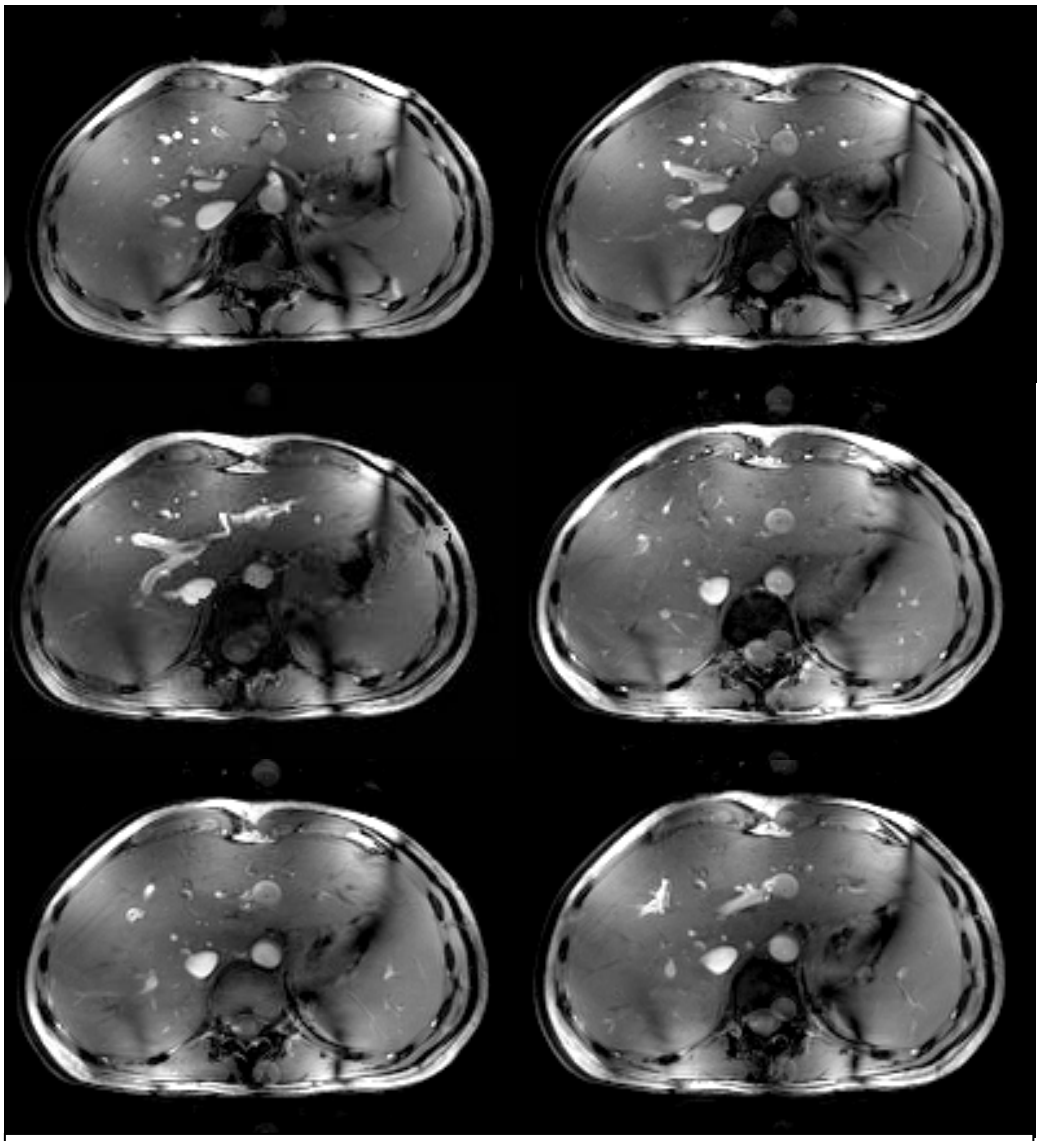

Figure 5.4 – GRE, TR/TE=75/4.0 ms, 1.4 x 1.4 x 3.0 mm resolution, breath-held (20 sec) with visible destructive interference and a flow artifact from the aorta (anterior)

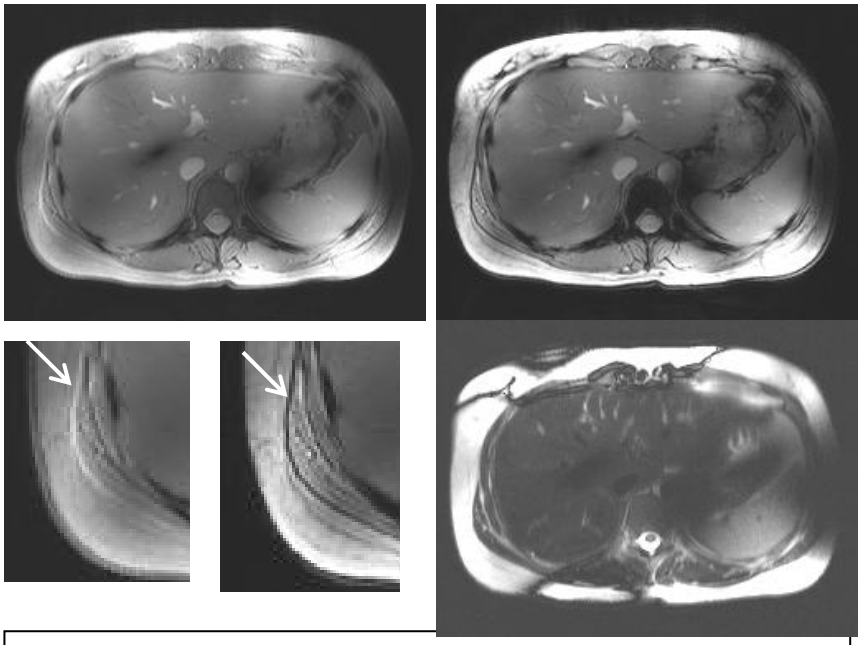

Figure 5.5 – In and out of phase GRE 2D multi-slice images on the left and right respectively on top and in bottom left corner. In the lower right corner is a HASTE (Half-Fourier acquired single-shot turbo spin echo) image with TE = 152 ms.

5.3 Spectroscopy

Background

Both *in vivo* and *in vitro* ^{1}H MRS have proven effective in distinguishing the distinct biochemical characteristics of malignant tumors relative to benign lesions or normal tissue. Particularly, higher concentrations of choline-containing compounds are found in malignant tumors with a positive correlation between [tCho] and metastatic potential which has been demonstrated in a number of cancers including breast, brain, prostate, spleen, colon, and liver (62). A very important finding came from de Molina et al. demonstrating that choline activation is necessary and sufficient for proliferation of mammary epithelial cells and tumor progression in response to growth factors (63). Researchers have shown that ^{1}H MRS can detect changes in the metabolite spectrum over

the course of chemotherapeutic treatment and may be able to indicate the effectiveness of a particular type of chemotherapeutic agent within 24 hours after the first dose (64). In contrast, the current standard way to gauge effectiveness is by observing tumor shrinkage by imaging with mammography, ultrasound, or MRI, which can only detect effectiveness after several weeks.

As with primary site tumors, malignant tumors in the liver tend to have a higher concentration of choline-containing compounds than benign lesions or normal liver tissue. Most of the studies on MRS of liver cancer have studied hepatocellular carcinoma (HCC) rather than metastatic liver disease, however the HCC studies are important to the study of metastatic disease in that organ-specific techniques will be shared. Bell and Bhakoo used *in vitro* and *in vivo* ^{31}P MRS to detect phosphocholine (as well as phosphoethanolamine) and collected previously published ^{31}P MRS data about hepatic carcinomas (65). Their research supports the findings from ^{1}H MRS that phosphocholine is elevated in carcinomas of the liver including HCC and metastatic lesions. Two papers from the same group demonstrate use of *in vivo* ^{1}H MRS for detecting changes in choline-containing compounds in HCC with a 3 T scanner before and after chemotherapy (60,66). Since the elevation of [tCho] is correlated to malignancy and metastatic potential in many solid organ cancers the behavior of metabolic profiles of the metastases of those cancers would also be of interest. Analyzing the change in the metabolic spectra of metastases over the course of chemotherapeutic treatment is important for determining the response of the cancer cells in the target organ, which is indicative of the response of the other metastatic cells throughout the body that cannot be easily detected and located. Additionally, the primary tumor has typically been surgically removed by this late stage

of the treatment, making it no longer an option for tracking therapeutic effectiveness. In these late stages, patients can ill afford time lost on ineffective chemotherapeutic treatments, so an early understanding of a particular cancer's response could expedite clinical decisions about whether to continue the current therapy or pursue a different, possibly more aggressive, cancer treatment.

Methods

After collecting images for voxel planning, MRS was performed using a 30 x 30 x 30 mm voxel placed in the anterior right lobe of the liver. An 8-channel RF flexible body array was used. Spectra were acquired using a modified PRESS sequence, with respiratory triggering and water suppression. TR = 3000 ms, TE = 50 ms. The B_0 field was shimmed using the manufacturer's 3D phase map tool acquired during a breath-hold. Spectral acquisition was performed during consecutive sets of 20 s breath-holds (67) or by triggering with a respiratory sensor. Respiratory triggering was used for 64 excitations. The eight receive channels were combined using complex weighting by the first point of the FID.

Results

Spectra were successfully acquired during breath-holds or with triggering using the respiratory bellows. Spectroscopy was not successful in 2 of 4 subjects due to inability to shim B_0. The spectrum shown in Figure 5.6 has a broad linewidth, and better B_0 shimming methods are needed to improve the spectral quality. Nevertheless, some

metabolite resonances are visible in the 3-4 ppm range, with a probable choline resonance at 3.2 ppm.

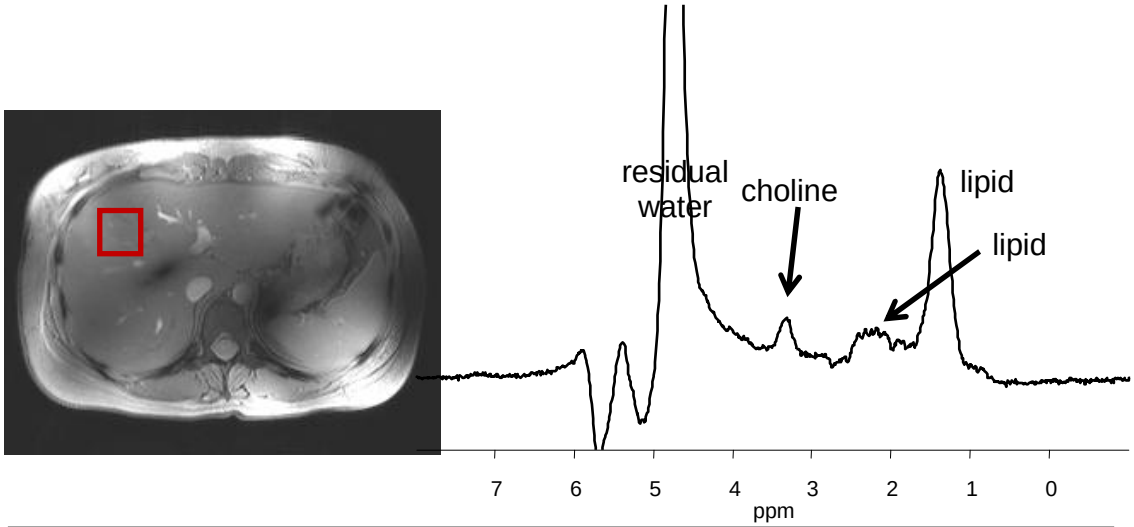

Figure 5.6- Single-voxel ^{1}H MRS (PRESS)

5.4 Acceleration

Liver imaging has much to gain from the improved parallel imaging that comes with increased field strength. As with many applications, higher spatial resolution is valuable for better identification of structures. Liver more than most organs benefits from reduced scan times for the acquisition of images during a single breath held for a reasonable amount of time. To further investigate these potential gains, three experiments were conducted. One experiment was designed to explore how fast an image of reasonable quality could be acquired. Another was designed to determine the maximum attainable acceleration. The goal of the third experiment was to optimize resolution. Together the set of experiments is a preliminary characterization of the advantages derived from the parallel imaging improvement at 7 T.

Methods

The previously described 16-channel flexible body surface array and associated hardware were used in transmit and receive with the aforementioned B_1^+ shimming algorithm. Healthy volunteers were studied under a protocol approved by our institution's IRB. Multi-slice gradient recalled echo (GRE) images were collected without acceleration and with 1-dimensional reduction factors of 2, 4, and 8 (data not shown), keeping all other parameters equal for the temporal resolution scans (Figure 5.7).

To evaluate g-factors of various accelerations, images and corresponding g-factor histograms and maps were obtained (Figure 5.8). Three-dimensional GRE images with different accelerations were acquired with read-out in the anterior/posterior (AP) direction. The accelerated scans were acquired with resolution = 0.9 x 0.9 x 5.0 mm (matrix = 256 x 256 x 16), and the unaccelerated scan was acquired with = 2.5 x 1.4 x 5.0 mm (matrix = 256 x 141 x 16). Each acquisition was collected during a single breath-hold (TE = 1.6 ms, TR = 3.3 ms). Scan times were recorded without including the time for reference scans. The dark area in the abdomen in the maps is susceptibility artifact from air. Consequently, the signal in this region is too low, so it was excluded from the calculations. Using the data shown in Figure 5.8, mean and maximum g-factors were calculated and plotted in Figure 5.9 with solid lines. In the same way that the right/left (RL) accelerations were acquired, but rotating the phase encode direction, AP accelerations were also acquired and plotted in Figure 5.9 with dotted lines. Reconstructions were done offline with software developed in-house with separate acquisitions for estimating the generalized autocalibrating partially parallel acquisitions (GRAPPA) interpolation weights (68).

For the spatial resolution scans (Figure 5.10), we increased the matrix size and decreased the field of view to achieve an effective acceleration factor of 6. The manufacturer's GRAPPA method was used for the improved temporal resolution and an offline reconstruction was performed using opengrappa.m for the improved spatial resolution.

Results

Figure 5.7 shows that the time resolution can be increased using GRAPPA with reduction factors of 2 and 4 before seeing significant artifacts. In the results from evaluating the maximum possible acceleration are shown in Figure 5.8. The arrows in the images with accelerations of 6 and 8 show noticeable artifacts, indicating that this GRAPPA implementation fails at these high reduction factors. The histograms show the SENSE g-factor value distribution from the maps. The coil array used here is designed for high RL acceleration rather than AP. With this coil design it is not possible to do accelerations in the head/foot direction. With this coil design, accelerations up to 3 x 4 for 2 dimensions were obtainable with max g-factors under 1.5. For the spatial resolution scans (Figure 5.10), with increased spatial resolution, an 18x smaller pixel volume was achieved, and thus two individual vessels that could not be resolved in the image without acceleration could be seen clearly (as indicated by the arrows).

`

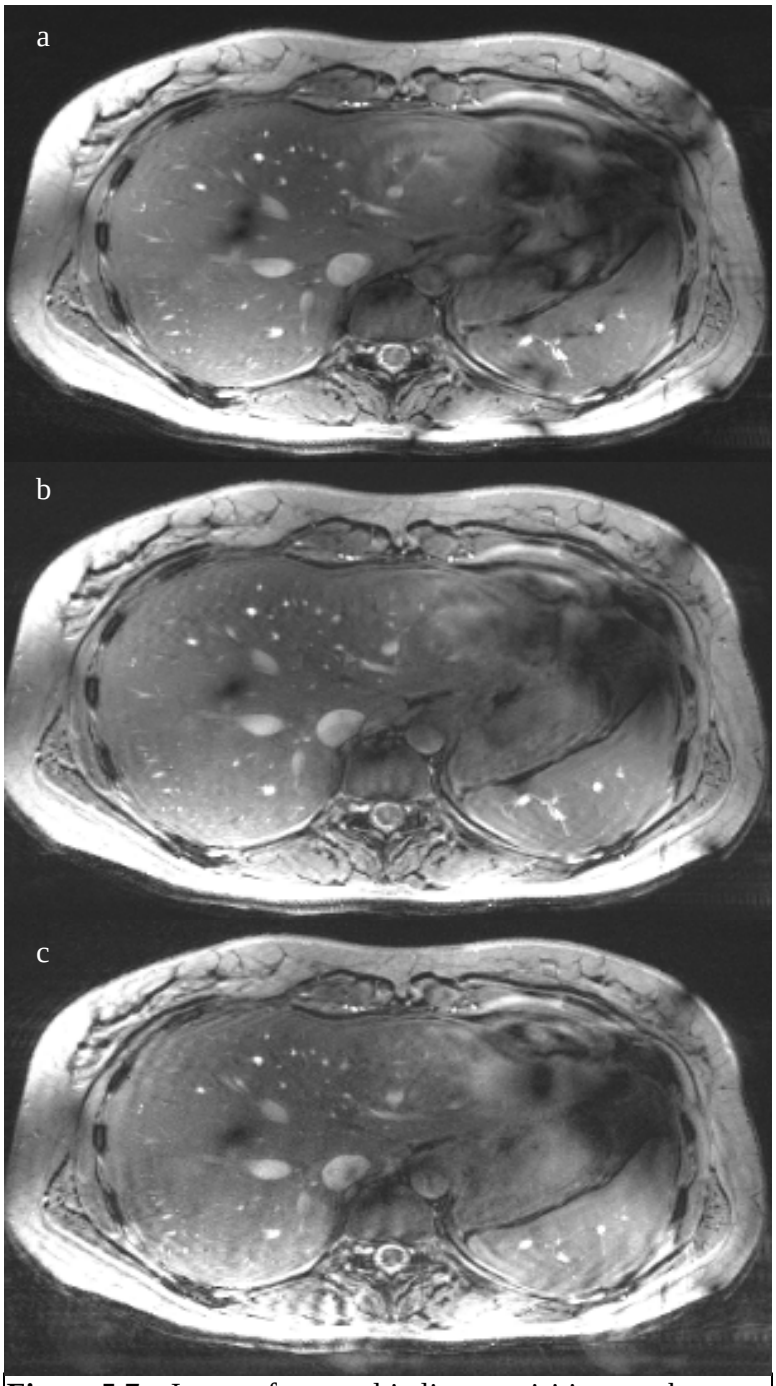

Figure 5.7 – Images from multi-slice acquisitions each collected during a single breath-hold (TE/TR = 4.04/25), a) no acceleration, 19 s; b) GRAPPA factor of 2, 11 s; c) GRAPPA factor of 4, 7 s

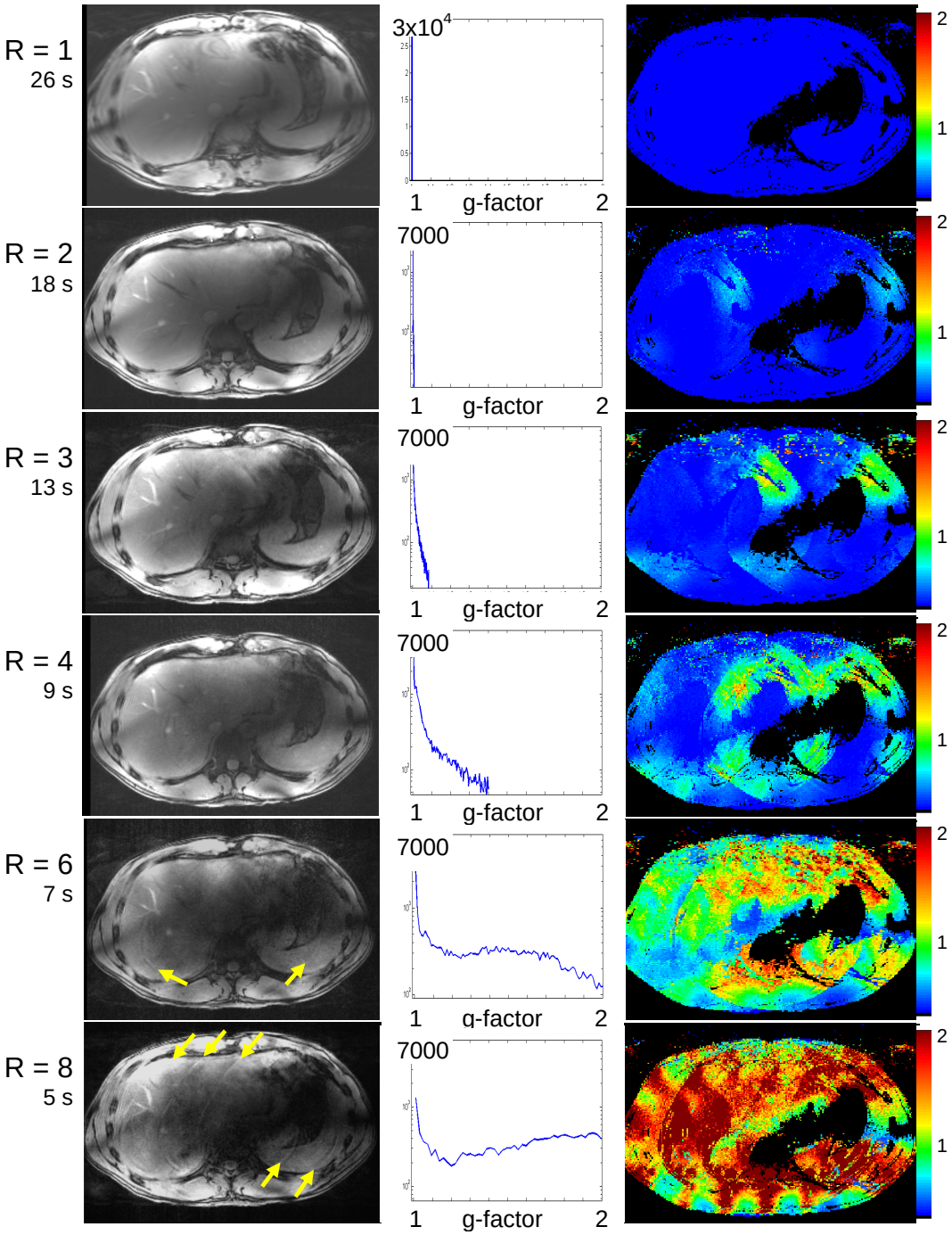

Figure 5.8 - Images and corresponding g-factor histograms (in voxels) and maps from 3D acquisitions. The g-factor histogram plots are logarithmic.

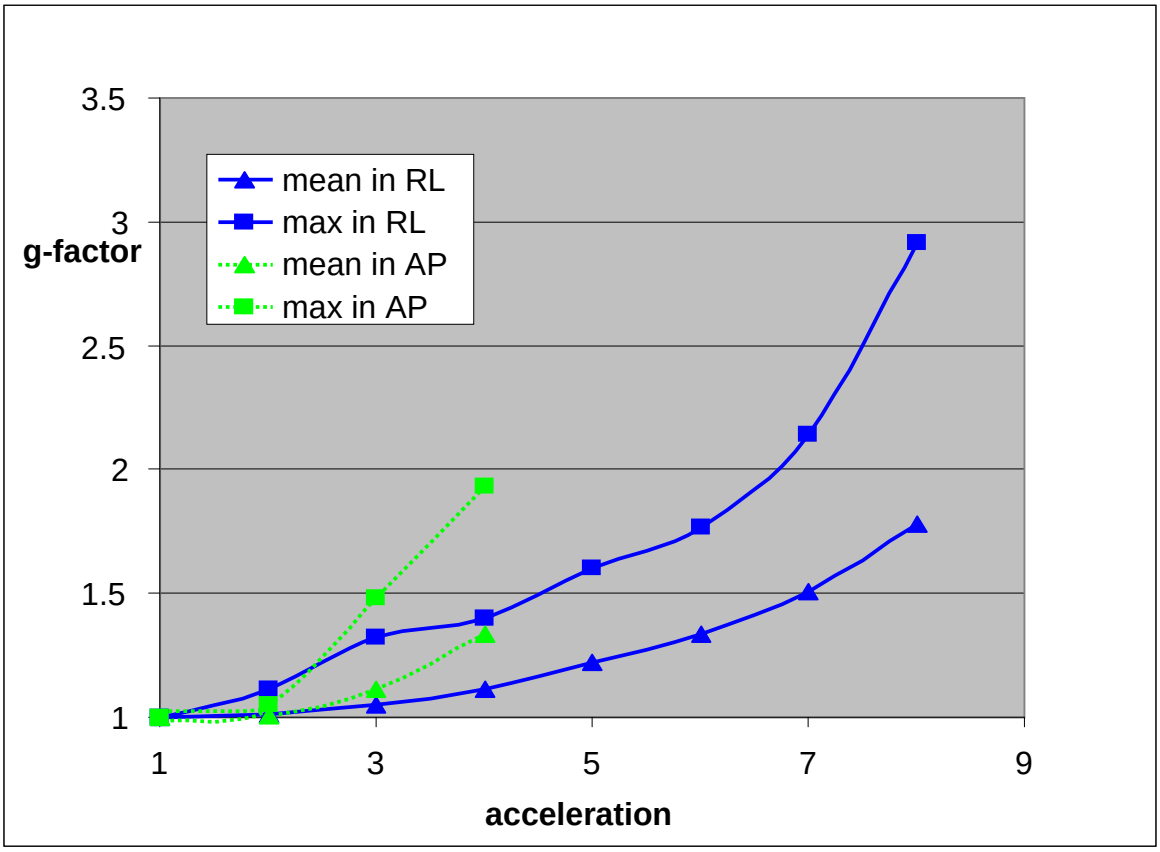

Figure 5.9 - Mean and maximum g-factors
The solid lines are from the maps in Figure 5.8, RL accelerations, and dotted lines are collected in the same manner but with the phase encode direction rotated for AP accelerations.

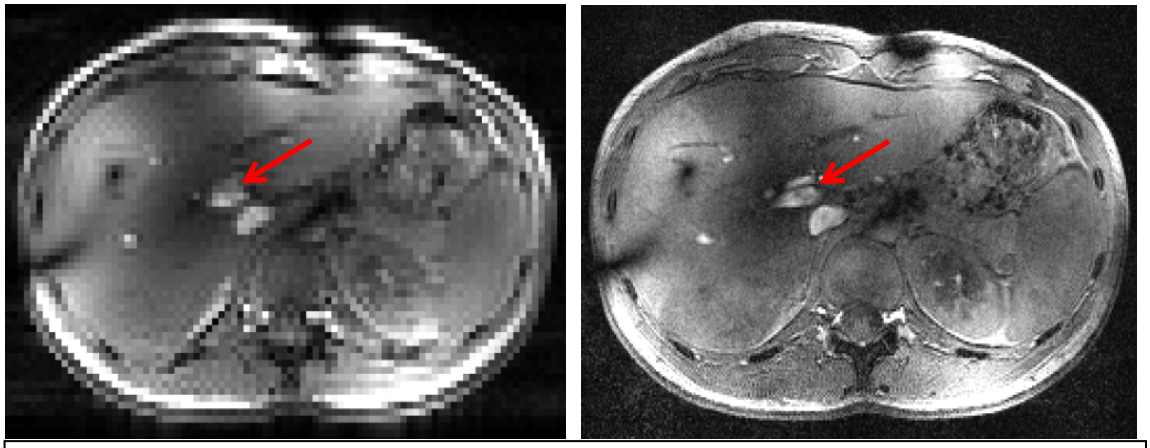

Figure 5.10 - 3D GRE images were collected during one 20 s breath-hold (TR = 6, TE = 3.1). The image on the right was collected with a reduction factor of R = 6 x 1, increasing the resolution from 3 x 3 x 5 mm (matrix = 128 x 128 x 32) to 1 x 1 x 2.5 mm (matrix = 384 x 64 x 32).

5.5 Discussion

These results demonstrate the feasibility of liver imaging and spectroscopy at 7 tesla. Acceleration possibilities and parallel imaging advantages at high fields are looking very promising. The primary areas that need further development are optimization methods for producing homogeneous B_1 fields for uniform excitation over the liver, and methods for localized B_0 shimming to improve spectroscopy linewidth.

While this work has shown that spectroscopy in the liver at 7 T is feasible, substantial technical improvements are needed to make it a reliable, practical tool for research. Current line widths are too broad due to the insufficient B_0 shimming. Better water suppression is also required before adequate spectra can be consistently acquired. Finally the available peak B_1^+ power can be a crippling limitation. Some of these issues can be

very manufacturer dependent, B_0 shimming and water suppression from software and B_1^+ and possibly B_0 shims from hardware. Moreover, most clinical platforms are tailored for imaging and suffer from underdeveloped spectroscopy functionality. However, as the demand for and prevalence of 7 T scanners continues to rise and the value of spectroscopy in a clinical setting becomes more evident, scientific development and manufacturer implementation can provide the tools to make a more robust system for spectroscopic development and application.

Parallel imaging performance for objects on the order of a human torso scales linearly with field strengths above 3 T. Imaging the liver at 7 T has potential for very high accelerations which can enable ultra-fast scanning with full volumetric coverage. However, there is still progress to be made. The phase-only B_1^+ shimming algorithm used here needs to be extended for homogenous excitation over large regions. Also, while increased noise with increased acceleration is in inherent in parallel imaging, the artifacts in accelerations above 6 suggest that different parallel imaging reconstruction algorithms may be required. Additionally this coil was designed for high accelerations in one dimension. Future designs could support higher accelerations in more dimensions.

Recently presented work confirms our results with similar performance for in-phase and out-of-phase fat and water imaging as well as showing very similar B_1^+ artifacts (55). Subsequent improvements in phased B_1^+ shimming are showing better homogeneity over larger fields of view. Also, a new method called Time Interleaved Acquisition of Modes (TIAMO) may prove beneficial for evening out inhomogeneities in larger areas of interest and has shown promising results in abdominal imaging at 7 T (42,47). Unfortunately there are notable time costs with TIAMO.

Chapter 6: Imaging the Uterus at 7 T

Significant contributions to this work were made by Shalom Michaeli.

Rapid progress in ultrahigh magnetic fields has been made, driven by the potential to provide higher SNR than lower fields. With such advances it is important to establish the feasibility of body imaging at 7 T and to assess the advantages of ultrahigh magnetic fields for clinical applications, both routine and exceptional. In uterine imaging conventional laboratory frame longitudinal, T_1, and and transverse, T_2, and novel rotating frame adiabatic $T_{1\rho}$, $T_{2\rho}$, and RAFF (Relaxation Along a Fictitious Field) forms of relaxation contrasts can be valuable not only for differentiating normal from abnormal tissue but also for distinguishing between the different layers of tissue within the uterus, which is of diagnostic importance in many diseases. This work demonstrates the feasibility of uterine imaging at 7 T, compares the performance to 3 T, and explores the contrast-to-noise ratio (CNR) from various types of contrasts at high fields.

6.1 Introduction

A 7 T body imaging system may be able to offer advantages over clinically available field strengths. Body imaging at high fields remained elusive until recently because of multiple experimental obstacles including susceptibility artifacts due to static magnetic field B_0 inhomogeneities and RF pulse field imperfections arising from constructive and destructive phase interactions. However, with the recent development of a comprehensive B_1-shimming procedure for the correction of phase, body imaging became more feasible

at high fields, providing possibilities for the study of benign and cancerous lesions with greater temporal, spatial, and spectroscopic resolution at 7 T (26,45). In addition to the SNR gains, contrast mechanisms may behave differently in a stronger B_0 field. Understanding T_1 and T_2 contrasts in the uterus at 7 T has high relevance for understanding its possible role in clinical imaging. However, other forms of contrast are also important to explore, such as a novel adiabatic rotating frame relaxation method and Relaxations Along a Fictitious Field (RAFF) (69). This method comprises both longitudinal and transverse rotating frame relaxation pathways, $T_{1\rho}$ and $T_{2\rho}$, respectively (70). This rotating frame technique could provide unique tissue contrast from the conventional free precession T_1 and T_2 methods. This study establishes the framework for performing clinically relevant measurements at 7 T to assess the advantages of ultrahigh magnetic fields in imaging of the uterus.

Preoperative staging of endometrial carcinoma is an important clinical application of MRI for determining the depth of tumor invasion into the myometrium, which is correlated with outcome (71). The use of gadolinium-based contrast agents aids in assessment of the tumor volume and vascularization with dynamic contrast enhancement (DCE) which would benefit from the time resolution possible at high fields with parallel imaging (72). Another clinically relevant role would be aiding in the diagnosis of adenomyosis, especially in distinguishing it from endometriosis, which presents with very similar symptoms.

Beyond cancer, high field MRI may also be of benefit in the effort to understand infertility. With increased SNR both imaging and spectroscopy could be used to evaluate the endometrial lining and increased temporal resolution could be used to capture uterine

peristalsis which is known to play an important role in fertilization. A variety of forms of contrast could be particularly useful for non-invasively evaluating endometrial tissue. The highly dynamic nature of the endometrium through out the menstrual cycle makes it both challenging and exciting to study. Throughout the cycle, the tissue changes thickness, density, water content, and ratio of bound water to free water, all of which can be measured with MRI relaxation methods.

6.2 Establishing Feasibility and Framework

Methods

Studies were conducted on a 7 T whole-body magnet (Magnex Scientific, Oxfordshire, UK) with a Sonata gradient system and TIMS console (Siemens Medical Systems, Erlangen, Germany). An 8-channel TEM/stripline flexible body transceiver array was used for imaging (44). An algorithm for B_1 shimming was employed for the removal of destructive interference from the area of interest, significantly improving the imaging as shown in Figure 6.1 (26,45). Both gradient echo (GRE) and T_2-weighted turbo-spin echo (TSE) images were collected. The gradient echo (GRE) images were collected with TR/TE = 50/4.1 ms, 3.0 mm slice thickness, matrix = 512 x 512. The TSE imaging was performed with TR/TE = 5000/143 ms, 2.0 mm slice thickness, and matrix = 512 x 512 (Figure 6.1). Images were obtained both in the sagittal plane and transverse along the length of the uterus, a view important for determination of invasion of endometrial cancer into the transitional zone and myometrium. Clinically this same transverse view is later valuable for histological comparison following hysterectomy. Figure 6.3 shows these two orientations collected with a TSE sequence with TR = 137 ms. On the left is a sagittal

view with TR = 5220 ms. On the right is a transverse view with inversion recovery TI = 23 ms and TR = 7000 ms.

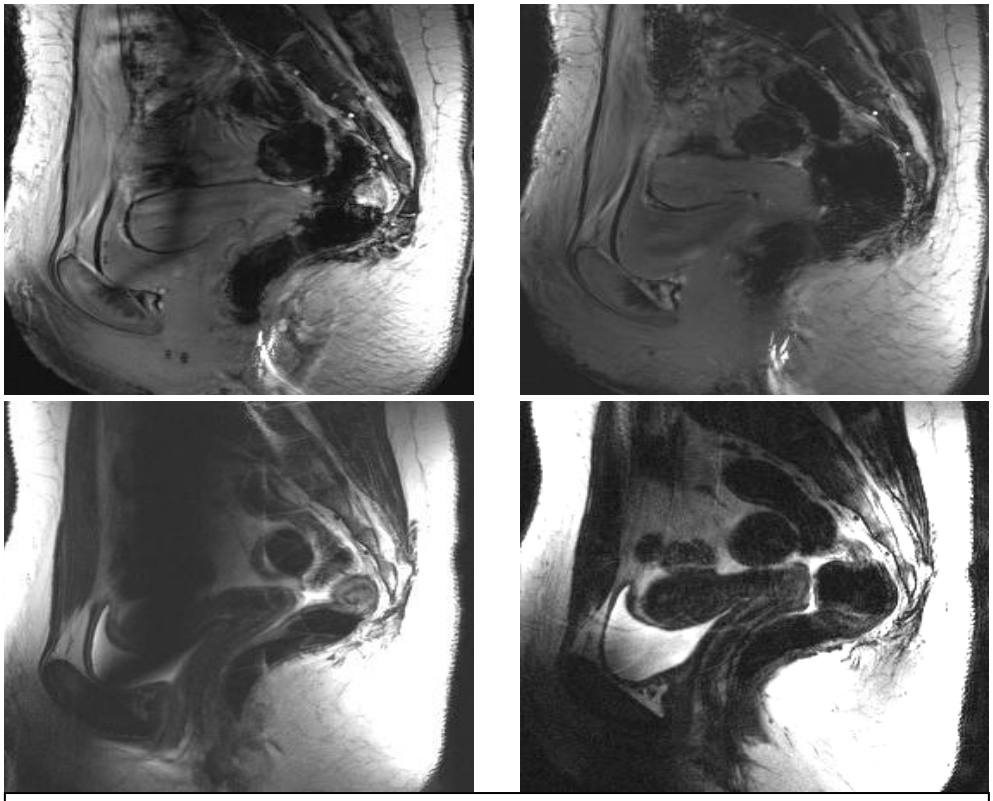

Figure 6.1 – The images on the left show GRE (top) and TSE (bottom) before shimming, the artifacts indicated by the arrows. The images on the right show the same images after applying B_1 phase shimming.

Results

Utilization of the conventional GRE and TSE pulse sequences at 7 T with no B_1^- shimming algorithm was found inadequate because of the phase artifacts, which were successfully removed using the B_1-shimming procedure (Figure 6.1). However, with the phase correction a relatively cancelation-free image could be produced in most cases and

a high-quality image could be produced with clear differentiation between the endometrium, transitional zone, and myometrium as shown in Figure 6.2 and Figure 6.3. Clinically important forms of contrast and orientations were demonstrated at 7 T. T_2-weighted MRI provides the greatest anatomical differentiation. However, the GRE images remain important for their clinical role in fast DCE applications.

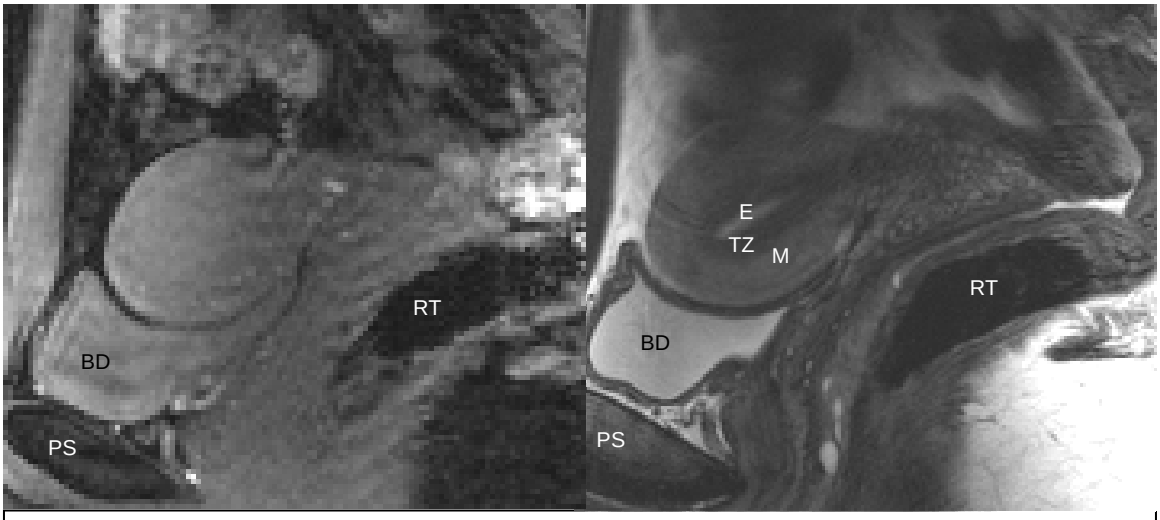

Figure 6.2 – The right-hand image is a GRE collected with TR = 35 ms and TE = 4 ms. The left-hand image was obtained using a TSE sequence with TR = 5220 ms and TE = 143 ms

BD - bladder	E - endometrium
PS - pubic symphysis	TZ - transitional zone
RT - rectum	M - myometrium

6.3 Field Comparison: 3 T vs. 7 T

The purpose of this study is to compare 7 T and 3 T *in vivo* MRI of the uterus. To that end, images from the same subject on each scanning system can give useful images for qualitative analysis. These same images can be used for a quantitative comparison by

measuring the CNR. Additionally, it would be useful to obtain relaxation maps of the uterus to better understand relaxation rates at 7 T.

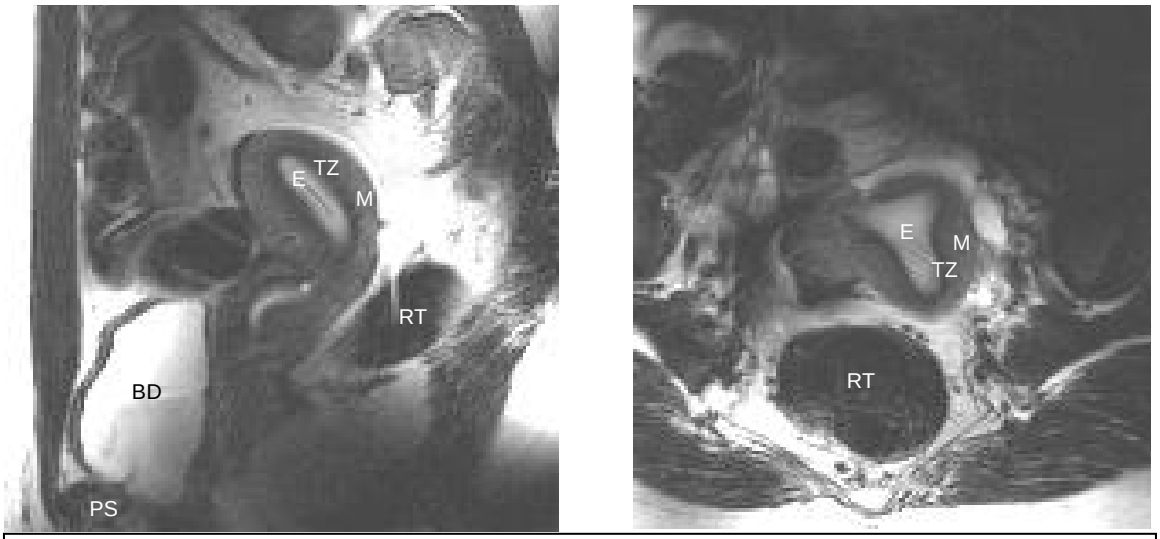

Figure 6.3 – Sagittal T_2-weighted TSE TE/TR = 137/5220 ms on the left and transverse T_2-weighted TSE with inversion recovery TE/TR = 137/7000 ms, TI = 23 ms on the right

BD - bladder	E - endometrium
PS - pubic symphysis	TZ - transitional zone
RT - rectum	M - myometrium

Methods

Four normal volunteers were scanned at both 3 T and 7 T. Scans at both fields were conducted within 24 hours or were taken at the same point in the menstrual cycle. On a Siemens 3 T Trio MR scanner, an integrated body coil was used in transmit, and an 8-channel surface array coil was used for receive. On a 7 T Magnex magnet with a Siemens console, the aforementioned 8-channel body surface array with TEM/stripline elements was used to transmit and receive. The phase of each channel was optimized *in vivo* using the B_1 shimming algorithm previously mentioned. On both scanners, GRE and TSE

images were collected. GRE images were collected with a slice thickness of 3.6 mm. The timing parameters at 3 T were TR = 100 ms and TE = 10 ms and at 7 T, TR= 28 ms and TE = 4.5 ms. TSE images were collected with a slice thickness of 3.0 mm. For TSE the timing parameters at 3T were TR = 6700 ms and TE = 117 ms and at 7 T, TR= 5220 ms and TE = 138 ms. The CNR was determined using the contrast between the endometrium and the inner myometrium. The 3 T images were collected with a 256 x 256 matrix, and the 7 T images were collected with a 512 x 512 matrix. No intensity correction was applied to the 7 T images. The data from all of the subjects was combined. ROIs for each of the tissue types were manually selected.

In addition to the CNR comparison, T_2 values at 7 T were explored. Figure 6.5 shows a T_2 map obtained on the 7 T system, showing the T_2 values of the normal uterine layers in addition to the T_2 values of two abnormal lesions (incidental in a normal volunteer). ROIs were selected and a relaxogram made as shown in Figure 6.6, relaxogram above, ROIs below.

Results

Even without a patient population, we were able to evaluate some abnormal lesions in the uterus for our field comparison. Nabothian cysts and fibroids are common benign uterine lesions. Of the normal volunteers scanned at both 7 T and 3 T, two had identifiable Nabothian cysts and one had fibroids which were later confirmed with clinically biopsy. In Figure 6.4, the top two images are gradient echo images, and the rest are SE images. The T_1-weighted images do not illuminate the structure as well as the T_2-weighted images. The images on the left were collected at 7 T, and those on the right were

collected at 3 T on the same subject. Fibroids can be seen in the myometrium (Lyomyoma) and endometrium (endometrial polyps). Nabothian cysts appear near the cervix. The image on the right captures the correct slice for seeing the cysts. Upon visual inspection, the anatomy is clearly visible at either field strength. Some B_1 artifacts remain in the 7 T image even after application of the B_1 shimming phase corrections. The combined subject data showed the average CNR at 7 T was 7.6, and the average CNR at 3 T was 4.06, which indicates that tissue differentiation between the endometrium and myometrium improves with field strength, while overall image quality still suffers a bit at 7 T due to B_1 inhomogeneity issues. The T_2 values obtained from the T_2 maps have clear differentiation of the relaxations of the tissue types. The T_2 of the endometrium is approximately 145 ms (though this changes with menstrual cycle phase). The T_2 of the transitional zone is approximately 95 ms. The T_2 of the uterine fibroid is in the range of 85-100 ms.

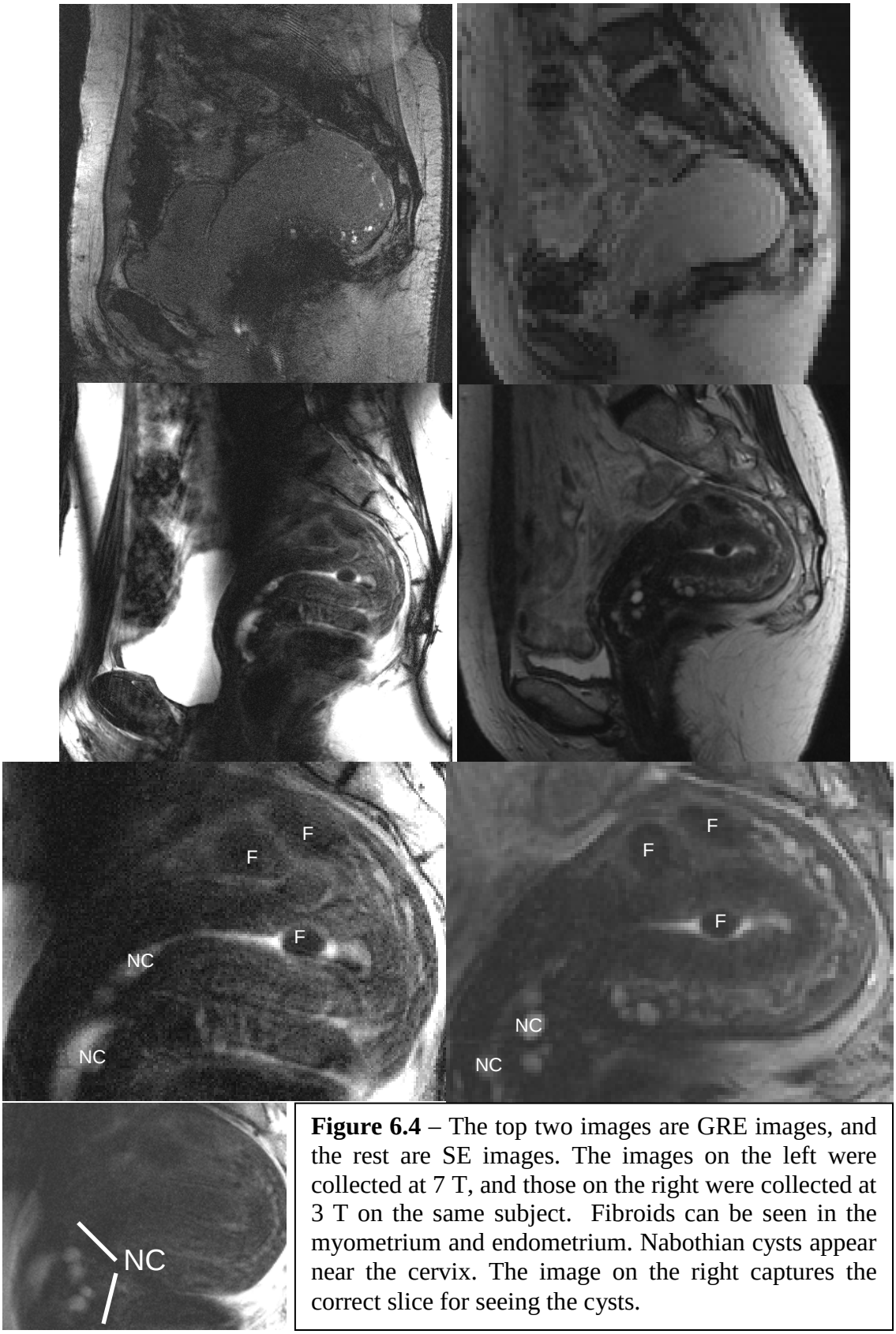

Figure 6.4 – The top two images are GRE images, and the rest are SE images. The images on the left were collected at 7 T, and those on the right were collected at 3 T on the same subject. Fibroids can be seen in the myometrium and endometrium. Nabothian cysts appear near the cervix. The image on the right captures the correct slice for seeing the cysts.

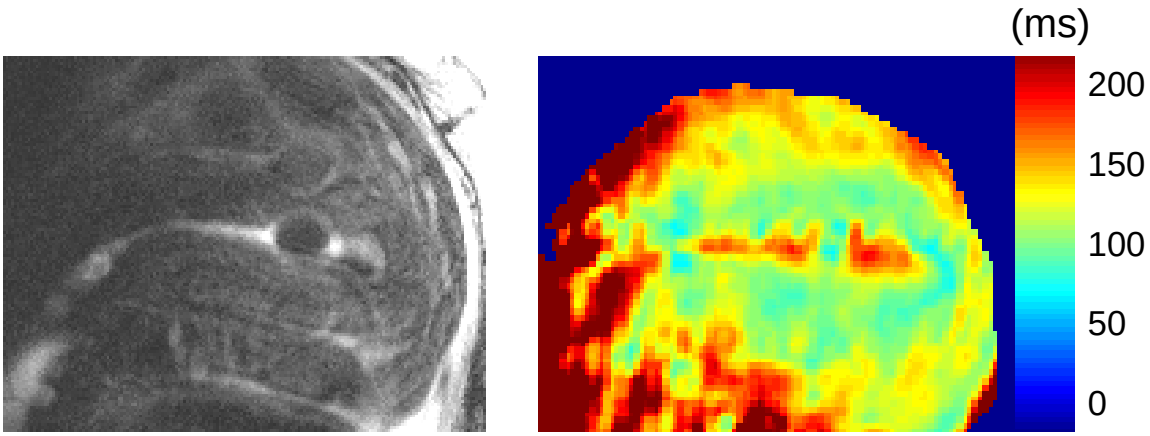

Figure 6.5 – From the same subject as in Figure 6.3 a T_2 map was collected at 7 T. The T_2 weighted image on the right is for anatomical comparison.

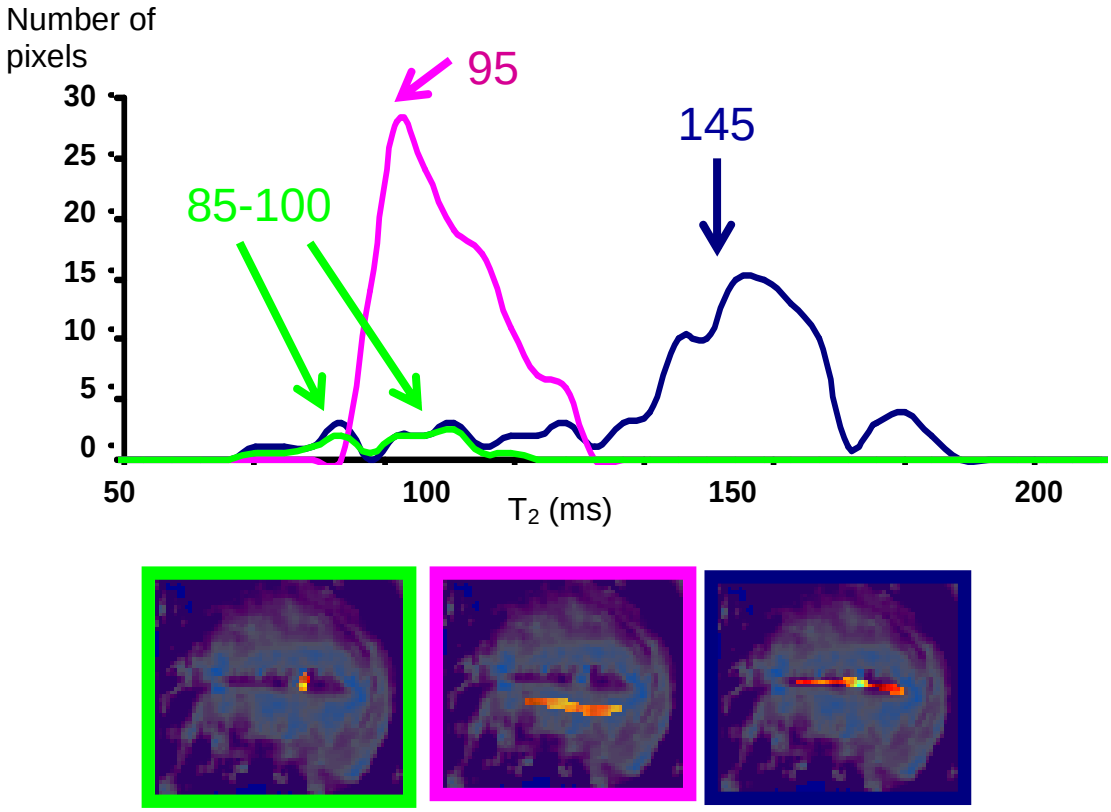

Figure 6.6 – A relaxogram generated from the T_2 map above (Figure 6.4) showing the T_2 distribution in the endometrial fibroid, the transitional zone, and the endometrium (including the fibroid). The regions of interest selected are shown

6.4 Tissue Contrast

Theory

The rotating frame relaxation mapping method in MRI is an attractive candidate to probe body pathology. The utility of $T_{1\rho}$ and $T_{2\rho}$ relaxation measurements to probe low frequency component of tissue spectral density function at high magnetic fields was recently extensively studied (70). The application of the conventional continuous-wave (CW) spin-lock (SL) rotating frame relaxation methods to generate tissue contrast is limited because of several technical obstacles, including B_0 and offset artifacts. Recently, it has been shown that adiabatic pulse sequences allow generation of contrast based on the rotating frame relaxations during adiabatic full passage (AFP) pulses, which require significant peak-power to satisfy the adiabatic condition. Here a new rotating frame method entitled **R**elaxation **A**long a **F**ictitious **F**ield (RAFF) has been employed for the imaging of the endometrium at 7 T (69). Since this method has lower peak-power requirements than other rotating frame relaxation methods, it is of particular interest at very high magnetic fields where increased SAR limits maximum peak-power. The method is based on frequency swept pulses with *sine* and *cosine* amplitude and frequency modulation functions with equal amplitudes, operating in the non-adiabatic regime. The relaxations during RAFF are governed by the contributions from both $T_{1\rho}$ and $T_{2\rho}$ relaxation channels. Because the method comprises $T_{1\rho}$ and $T_{2\rho}$ relaxations, the sensitivity of this technique has the potential to better differentiate tissue microstructure. Here we evaluate the potential for applying RAFF imaging to the uterus and compare RAFF to conventional contrast techniques.

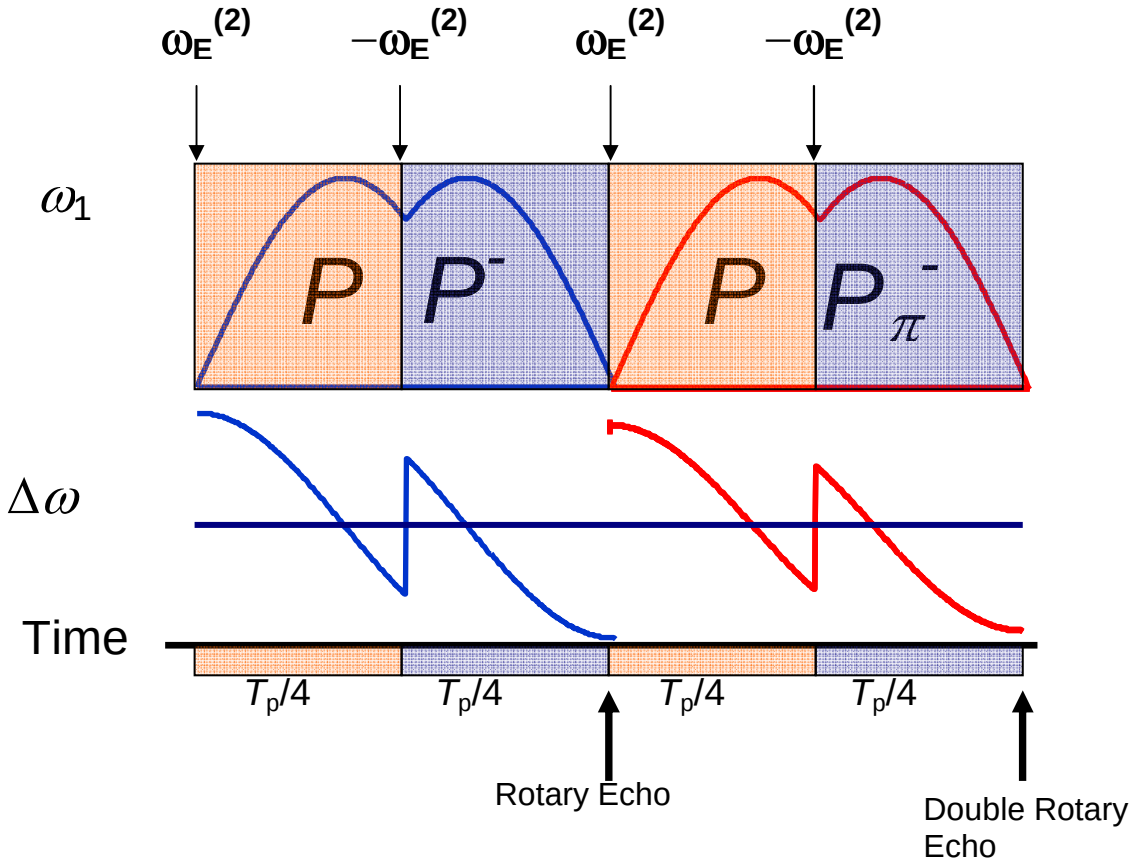

Figure 6.7 - Schematic diagram RAFF which generates rotary echoes in the high rotating frames using so called P-packets, which include a pulse (P), pulse reverse (P-), then a shifted pulse (P), and pi-shifted pulse reverse (P_{π}-), producing double rotary echoes. The pulse pairs are used to best return magnetization to the z axis.

Methods

Studies were conducted on a 7 T whole-body magnet (Magnex Scientific, Oxfordshire, UK) with a Sonata gradient system and TIMS console (vb13, Siemens Medical Systems, Erlangen, Germany). A 16-channel TEM/stripline flexible body transceiver array was used for imaging, each channel driven by a 1-kW amplifier with phase and gain control

(44). As with previous experiments, an algorithm for B_1^+ shimming was employed for the removal of destructive interference from the area of interest. T_1, T_2, and RAFF maps were collected in the sagittal plane (Figure 6.8) as well as transverse maps perpendicular to the long axis of the uterus (Figure 6.9). Both T_1 and T_2-weighted maps were collected using sequences provided on the scanner by the manufacturer. The RAFF maps were obtained using frequency swept pulses having sine/cosine (SC) amplitude $\omega_1(t)=\omega_1^{max}/(2\pi)*\sin(\omega_1^{max}t)$ and frequency $\Delta\omega_1(t)=\omega_1^{max}/(2\pi)*\cos(\omega_1^{max}t)$ modulation functions as shown in Figure 6.7. Here ω_1^{max} is the maximum amplitude of the RAFF pulse. The decay of the signal intensity (SI) was obtained by incrementing the number of SC pulses in the pulse train. The SI decay times used for the RAFF mapping were: 18, 36, 54, and 72 ms.

Results

In Figure 6.8 the RAFF, T_2, and T_1 maps (top) and images (bottom) are shown. The endometrium can be clearly distinguished in these images. It can be seen that the RAFF images and maps are artifact-free. Additionally, the differentiation between endometrium and myometrium is comparable in the T_2-weighted and RAFF images and maps. The T_1-weighting shows less uterine layer contrast as compared to T_2 and RAFF. Transverse images and maps were obtained in the same way as those in Figure 6.8, but on a different subject and with a different orientation and higher resolution (Figure 6.9). Benign Nabothian cysts can be seen in the lower part of the image, near the cervix. These appear red in both the RAFF and T_2 maps. The RAFF map has twice the resolution of the T_2 map because the T_2 map requires significantly more time to acquire. Studies were

completed in 6 normal subjects, none on hormonal birth control. One of the subjects was amenorrheal and thus excluded in the statistical calculations. Relaxation maps were calculated offline using Matlab 7.1 software Aedes, Juha-Pekka Niskanen. ROIs were drawn on all maps. Plots of relaxation rate constants and intra-subject contrast were generated and are shown in Figure 6.10. The ratio of relaxation values in the endometrium and transitional zone (E/T) and the myometrium and transitional zone (M/T) are important for differentiating normally occurring layers. The endometrium to myometrium (E/M) contrast is often important in diagnosing disease states such as endometriosis. The plot on the left shows the relaxation values obtained by selecting ROIs on the maps. The plot on the right shows the contrast between different tissues within the same subject.

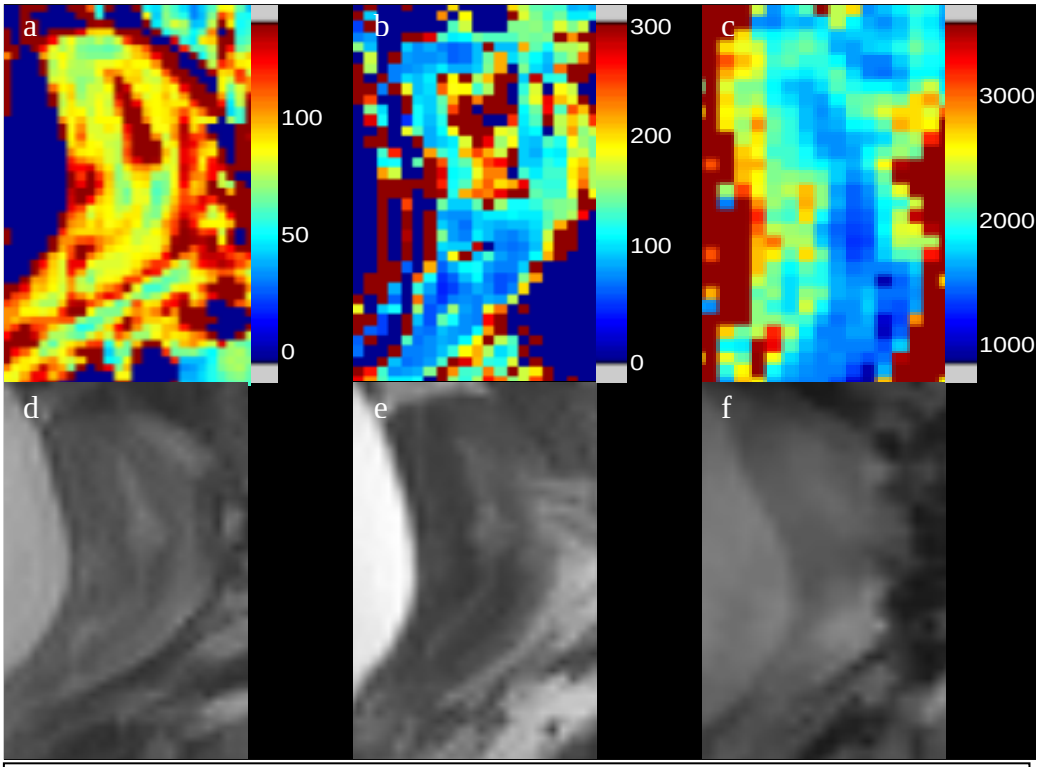

Figure 6.8 – Sagittal maps and images collected at 7 T as follows a) RAFF map, b) T_2 map, c) T_1 map, d) RAFF image, e) T_2-weighted image, and f) T_1-weighted image

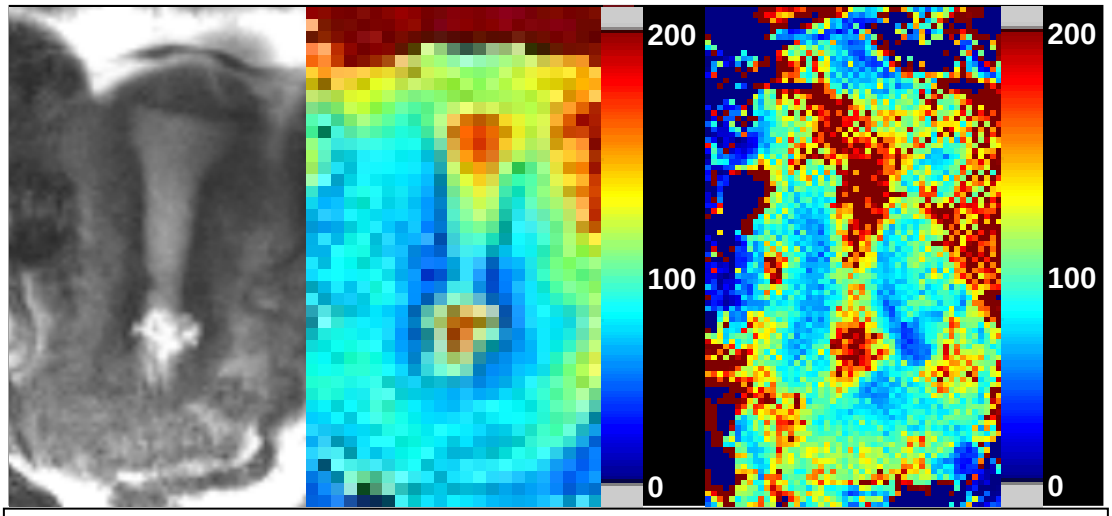

Figure 6.9 – All collected along the long axis of the uterus, on the left is TSE image. The center and right are T_2 and RAFF maps respectively. Benign cysts can be seen in the lower part of the image, near the cervix. The RAFF map has twice the resolution of the T_2 map because the latter requires significantly more time to acquire.

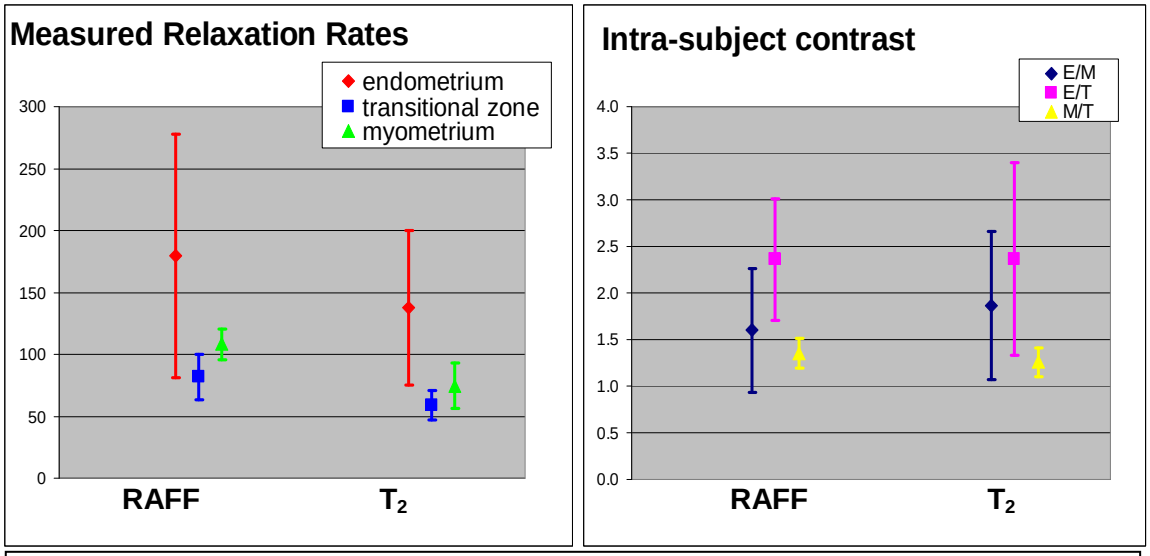

Figure 6.10 – Plots of relaxation rate constants and intra-subject contrast
The plot on the left shows the relaxation values obtained by selecting ROIs on the maps. The plot on the right shows the contrast between different tissues within the same subject.

6.5 Discussion

High-field magnetic resonance imaging provides high spatial and temporal resolution images with tissue differentiation in the uterus. Through further developments in B_1 shimming and protocol design are needed, 7 T has here been shown to be a promising platform for the study of the uterus. The increase in SNR improves tissue differentiation. Also uterine imaging may be an important application for the RAFF relaxation method, which is comprised of contributions from both $T_{1\rho}$ and $T_{2\rho}$ relaxation pathways. Even with our limited pool of subjects, RAFF appears to give contrast comparable to T_2 mapping in less time. The RAFF technique may ultimately provide a unique contrast from T_1 and T_2 in MR imaging, possibly improving diagnosis and opening new means to better understanding infertility especially through monitoring changes in the structure of the endometrium. While we have experimentally validated that the CNR for differentiating the endometrium from the myometrium is higher at 7 T than at 3 T, as theoretically expected, technical issues still confound efforts to transition 7 T scanners to a clinical setting, including residual B_1 inhomogeneities even after phase shimming and the necessity of manually tuning and matching RF channels individually. However, 3 T MR scanners are becoming increasingly popular for their advantages over lower field strengths, an encouragement that with more time and technical improvements 7 T scanners may become clinically viable tools for aiding diagnostic efforts.

Chapter 7: SWIRLY - Spatiotemporal-encoding with Incremental Refocusing along a trajectory

A frequency-swept RF pulse and modulated gradients can be used to move a resonance region through space to generate sequential excitation and subsequent echo formation with time-dependence, which allows image formation without use of the Fourier transform. This **s**patiotemporal encoding **w**ith **i**ncremental **r**efocusing a**l**ong a trajecto**r**y (SWIRLY) has the unique and important property that each region in space can be treated independently. Such spatial independence has potential to be of great benefit in applications that are inherently spatial in nature, such as compensating for inhomogeneous B_1 and B_0, which is of increasing interest for higher field strengths.

7.1 Introduction

Spatiotemporally-encoded MRI has been implemented in several forms and demonstrated notable advantages over classic frequency and phase encoding in particular applications. Early inspiration for spatiotemporal encoding came from Pipe's presentation of the quadratic phase profile with a frequency sweep and its utility for slice selection (73,74). Around that time Meyerand and Wong proposed a time-encoded method for imaging (75). Similarly, time encoding was increasingly recognized and utilized in spectroscopy through the work of Frydman and his research group. Use of time encoding for 2D, and later nD, NMR spectra substantially shortened acquisition times by obtaining the spectral information in a single scan (14,17). The effective application of this concept in imaging

followed shortly (10,15,16). The objective of much of this spatiotemporally-encoded imaging has been single-shot imaging for rapid acquisition, applications being those traditionally dominated by echo-planar imaging (EPI). EPI is vastly important and widely used for clinical and research applications but is haunted by substantial artifacts, motivating exploration of new ultra fast methods such as spatiotemporal encoding. There are a few variations in time-encoded sequence design. The Frydman group has produced a body of work on the use of time encoding in place of frequency encoding (11-21). Chamberlain et al. instead replaced phase encoding with time encoding and introduced the use of two 180° pulses to generate the same effective TE across the image for improved T_2 contrast (10). Recognition and utilization of time-encoding's inherent advantages for B_1 inhomogeneity compensation have made it even more appealing as an alternative to EPI (13,19). New additional techniques for reconstruction of spatiotemporally-encoded images have also been introduced (12,76). A unique variation on these sequences is the concept of implementing them in an entirely spatiotemporal manner such that the use of the Fourier transform becomes unnecessary, whereas all of the previously mentioned implementations involve at least one dimension of frequency or phase encoding. The use of a Fourier transform in even one dimension prevents these implementations from being purely spatial. A method for spatiotemporal imaging without a Fourier transform was described by Shrot, Tal, and Frydman (16,19). In this method, an excitation pulse is followed by two chirped inversion pulses along different axes, which essentially creates a spatial grid that can be "walked-through" using shaped gradients during acquisition, thereby obtaining the image without *k*-space. With this sequence they were able to demonstrate clear advantages for B_0 inhomogeneity compensation along one

dimension by modulating the pulse that generated that dimension of the grid, but expanding to more dimensions proved difficult (19). By extension, there would also be advantages for increasing B_1 homogeneity.

Described here is a new approach for entirely spatiotemporal image acquisition that remedies some of the challenges of the earlier method. This new sequence uses time encoding to produce an image by moving a resonance region along a 2D trajectory in space such that the excitation is itself spatially selective. Each region then can be refocused sequentially during acquisition, retaining the spatiotemporal independence that was established in the excitation. Accordingly, no Fourier transform is needed for reconstruction providing spatial independence in acquisition, and more interestingly the spatial independence of the excitation makes creation of highly tailored traversals of space possible, with inherent freedom facilitating unique treatment of each refocused region, rather than each grid dimension, giving substantially more control for compensating for multi-dimensional B_1 and B_0 inhomogeneities. Being that the resonance region is not sufficiently close to a delta function, reconstruction by merely rearranging the acquired signal to form an image is not ideal, even problematic. In this case an inverse problem solution is better suited to the reconstruction of the signal into an image. Importantly, working entirely in the spatiotemporal domain allows direct treatment of inherently spatial problems. This spatial independence is particularly unusual in MR imaging and thus opens opportunities for numerous novel applications that could not be considered with standard MR techniques.

7.2 Theory

Spatiotemporal encoding is generated by the application of a gradient in the desired encoding dimension which will impart a spatially-dependant range of frequencies. A concurrent RF excitation pulse with a chirped frequency sweep is applied. As the RF frequency is swept, the isochromats at each frequency will be perturbed into the transverse plane sequentially. The phase of each isochromat will be a combination of the phase acquired from the RF excitation and the phase accumulated while freely precessing after having been tipped into the transverse plane. By applying a gradient in the opposite direction the phase of each isochromat can be unwound sequentially. At any given time the isochromats that are in phase will contribute the majority of the signal. The signal can then be assigned to the corresponding spatial location.

Outer-volume-suppression techniques can be helpful to consider. In general, each band of suppression is achieved by selecting a set of gradients and an RF frequency offset to excite and then suppress a region of signal that is outside the region of interest. A series of bands are selected to surround the object of interest to suppress undesirable signal. Increasing the number of suppression bands can more accurately approximate a continuous suppression region. Instead of using constant gradients for each band a sine and cosine gradients could be employed to suppress a continuous ring of signal on the outside of a region of interest, such as suppressing the ring of signal from fat and skin surrounding the head (77). With a constant RF frequency, the ring will have a constant radius. However, if a frequency sweep were to be employed from the maximum offset to zero, then the continuously decreasing radius in the presence of sine and cosine gradients

would form a spiral. Rather than suppressing this spiral of excitation, the signal could be preserved, which is how the SWIRLY pulse sequence begins.

SWIRLY may be designed for many possible trajectories. For initial discussion, an Archimedean spiral with constant radial velocity over 2π radians is presented both for the simplicity of the geometric description and for the constant radial velocity. SWIRLY can be implemented in several forms as shown in Figure 1, including gradient echo (a), spin echo (b), double spin echo (c), and even as a variation of a (SWIFT) sequence (d), to give a few examples. In the Archimedean spiral trajectory, a frequency sweep consisting of a chirp-like pulse terminating at zero offset and keeping constant B_1 amplitude is applied concurrently with sinusoidal gradients on two axes offset one-quarter phase. The resultant trajectory is a spiral from the maximum radial distance to the center with constant angular and radial velocities. The frequency may similarly be swept from zero offset to the maximum frequency offset simply creating the spiral starting at the center and proceeding in the opposite direction. Since the B_1 amplitude is constant, $\alpha \propto (B_w/T)^{0.5}$ where α is the flip angle, B_w is the bandwidth and T is the duration of the excitation pulse. The distance from the center at any point along the trajectory r is proportional to the bandwidth, and consequently, taking the derivative with respect to time ($d\alpha/dt \propto 0.5*dr/dt$) clearly shows that constant B_1 plus constant radial velocity will produce a constant flip angle along the trajectory. The modulated gradients may initially appear to complicate many of the calculations shared by other time-encoded imaging, especially if attempting to consider one dimension individually. However, considering SWIRLY in polar coordinates will hopefully be more illuminating. Recasting in polar coordinates,

$$\theta = \begin{cases} \arctan\left(\dfrac{G_y(t)\omega(t)}{G_x(t)\omega(t)}\right) & \text{if } G_x(t)\omega(t) > 0 \\ \arctan\left(\dfrac{G_y(t)\omega(t)}{G_x(t)\omega(t)}\right)+\pi & \text{if } G_x(t)\omega(t) < 0 \text{ and } G_y(t)\omega(t) \geq 0 \\ \arctan\left(\dfrac{G_y(t)\omega(t)}{G_x(t)\omega(t)}\right)-\pi & \text{if } G_x(t)\omega(t) < 0 \text{ and } G_y(t)\omega(t) < 0 \\ \dfrac{\pi}{2} & \text{if } G_x(t)\omega(t) = 0 \text{ and } G_y(t)\omega(t) > 0 \\ -\dfrac{\pi}{2} & \text{if } G_x(t)\omega(t) = 0 \text{ and } G_y(t)\omega(t) < 0 \\ 0 & \text{if } G_x(t)\omega(t) = 0 \text{ and } G_y(t)\omega(t) = 0 \end{cases} \quad (1)$$

$$r = \sqrt{(G_x(t)\omega(t))^2 + (G_y(t)\omega(t))^2} \quad (2)$$

where G_x and G_y are the x and y gradients respectively and ω is frequency. For the Archimedean spiral form of SWIRLY, let g_{rot} be the desired degree of rotation along the spiral so that $G_x = A_x\cos(g_{rot})$ and $G_y = A_y\sin(g_{rot})$. Assume the gradients are chosen so that the maximum amplitudes of the x and y gradients are equivalent, $A_x = A_y = A_{xy}$. Equations 1 and 2 simplify to

$$\theta = A_{xy} g_{rot}(t) \quad (3)$$

$$r = A_{xy}\omega(t) \quad (4)$$

Looking at these equations notice that θ can be attributed to the action of the gradients, while r arises from the action of the frequency sweep. Defining the range of g_{rot} as 0 to 2π the angular term can be further simplified.

$$\theta = \frac{2\pi A_{xy}}{T} t \quad (5)$$

Since we have chosen an Archimedean spiral trajectory with constant angular and radial velocities and a chirp-like pulse

$$\frac{d^2\theta}{dt^2} = \frac{d^2r}{dt^2} = \frac{d^2\omega}{dt^2} = 0 \tag{6}$$

Which means that $\theta \propto r \propto \omega \propto t$. This relationship is of course very useful giving the ability to easily interchange with respect to which value a function is to be considered.

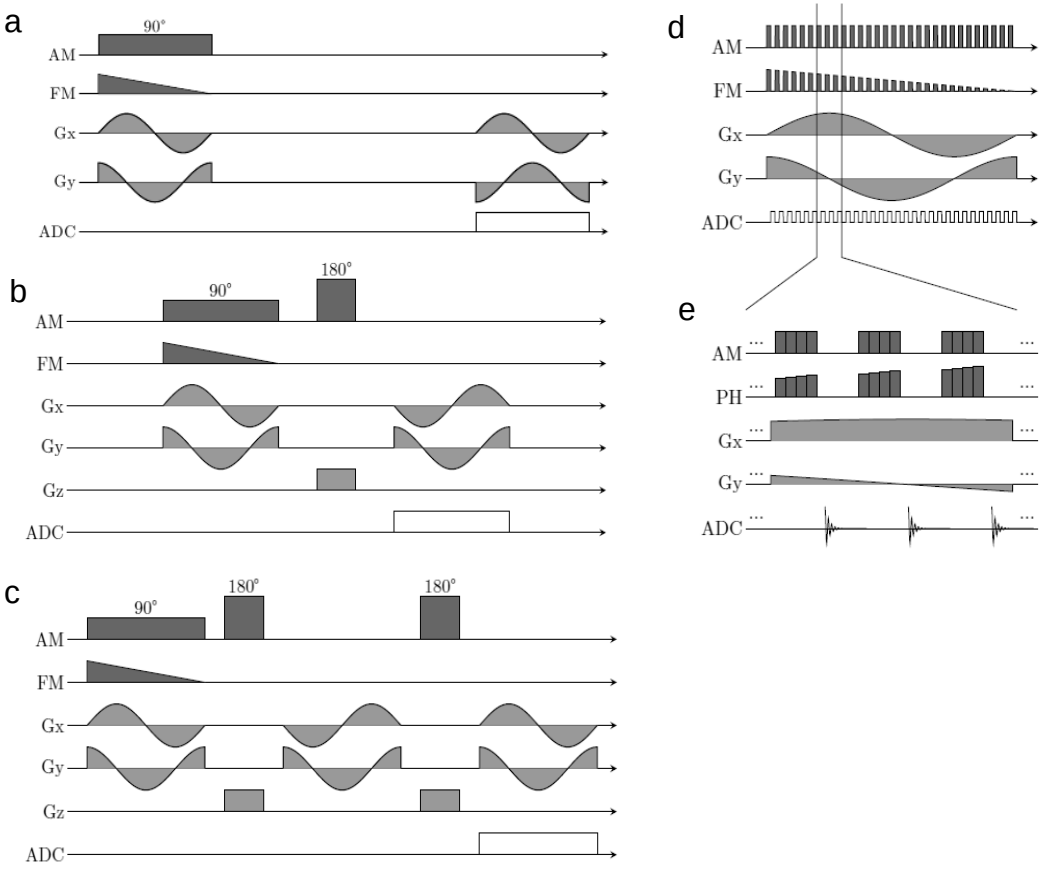

Figure 7.1 – Diagrams of GRE SWIRLY (a), SE SWIRLY (b), double SE SWIRLY (c), and SWIRLY SWIFT (d). A magnified portion of SWIRLY SWIFT is shown to better illustrate the gapping (e).

Imaging

In the case of the gradient echo (Figure 7.1a), repeating the sinusoidal gradients during acquisition allows for the sequential encoding of signal, not in the traditional form of a series of echos, but rather as a wave of signal arising from the spatially and temporally continuous nature of the frequency swept excitation. Now examining the spin-echo versions of SWIRLY (Figure 7.1b,c), one or more radio frequency 180° pulses may be applied to reverse the phase evolution, and at that time a slice selective gradient may be added. Looking particularly at the single echo implementation of SWIRLY, a hard pulse or sinc pulse is used for inversion in order to avoid introducing additional phase, whereas a double echo sequence opens RF pulse shape options to include adiabatic inversion pulses from the HSn family as the phase introduced by the first inversion pulse will be removed by the second (78,79). These adiabatic pulses bring advantages including uniform inversions even in the presence of RF field non-uniformities (7). Playing the excitation gradient shapes in reverse will result in the sequential phase refocusing along the trajectory in the opposite direction of the excitation. Much like the gradient echo form of SWIRLY, the resultant signal over time is not a classic echo, but rather a wave of echoes, which may be acquired during the application of this reversed set of gradient shapes in the single echo case, or again inverted and acquired during the application of a set of gradients matching the first in the double echo case. The double echo form shares the advantages RASER, including constant TE across the image and improved T_2 contrast. In addition to the gradient echo and spin echo versions of SWIRLY shown here, SWIRLY can also be implemented with a sweep imaging with Fourier transform

(SWIFT) acquisition method (80-85). An excitation pattern similar to the other implementations could be used expect with the introduction of gaps in the RF pulse during which time signal may be acquired for nearly simultaneous transmit and receive, bringing many of the unique and valuable properties of SWIFT into an entirely spatial domain (80-85). To better understand the gapping pattern, Figure e shows a zoomed portion of the sequence. The proportion of time that the RF pulse is turned on is called the duty cycle (dc). If the excitation and acquisition were truly simultaneous (rather than alternating) the duty cycle would be 1. With the currently available hardware a duty cycle of 0.25 is more reasonable for experiments and will allow enough time between excitation and acquisition for coil ring-down. (SWIRLY SWIFT is a misnomer in that reconstruction would still be done without a Fourier transform. However, the clarity this nomenclature brings to applications and advantages seems to outweigh the confusion that may be generated about the reconstruction.)

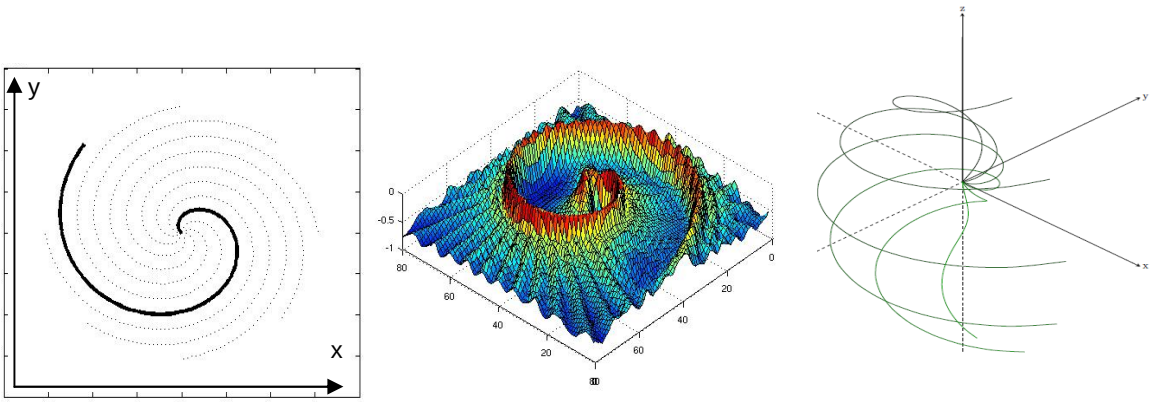

Figure 7.2 - The left-hand figure shows the rotation of trajectories to fill the 2D space. The center figure shows the inverse magnitude of the z magnetization from a simulation of SWIRLY excitation. The right-hand image shows SWIRLY trajectories for expanding SWIRLY to be a 3D sequence.

Repetition of the trajectory with different initial angles or phases of the gradients can be used to sufficiently cover a two-dimensional area as shown in Figure 7.2, which adds an additional term describing the degree of rotation θ_i onto equation (5) becoming

$$\theta = A/T*t*2\pi + \theta_i \quad (7)$$

The r term remains the same.

The sequential excitation and subsequent echo formation along the trajectory produce a time-dependant signal. The dephasing of signal from each isochromat is sufficiently rapid such that the maximum signal at a given time point can be attributed to the refocused isochromats, which can be thought of as a resonance region being moved through space. If the profile of the resonance region was so narrow as to be essentially equivalent to a delta function, reconstruction could be done by assigning temporal data to their corresponding spatial position along the known trajectory, thereby producing an image. However, this delta function assumption does not hold and thus neither does the geometric reconstruction; the characteristics of the resonance region require further discussion.

A frequency and amplitude modulated excitation pulse produces not a point but rather a forward-moving wave of excitation. This wave travels along a vector and excites a plane in space perpendicular to that vector. The RF pulse determines the velocity of the vector while simultaneous gradients can be used to control the direction of the vector. Considering a singular slice perpendicular to the plane simplifies this problem to a 2D situation; the wave is now a line of excitation traveling along an instantaneous vector. The simultaneous rotation induced by the gradients adds a rotational velocity that will be zero at the centriod (the point along the line that is on the spiral trajectory) and impart

more rotational velocity to the points along the line increasing with their distance from the centroid. The profile of the excitation along this line will determine the resolution of the image tangential to the trajectory of excitation. The point spread function will also be dictated by the profile perpendicular to the trajectory, or the cross-sectional profile of the moving line of excitation. Further, it is valuable to examine the profile along the path of

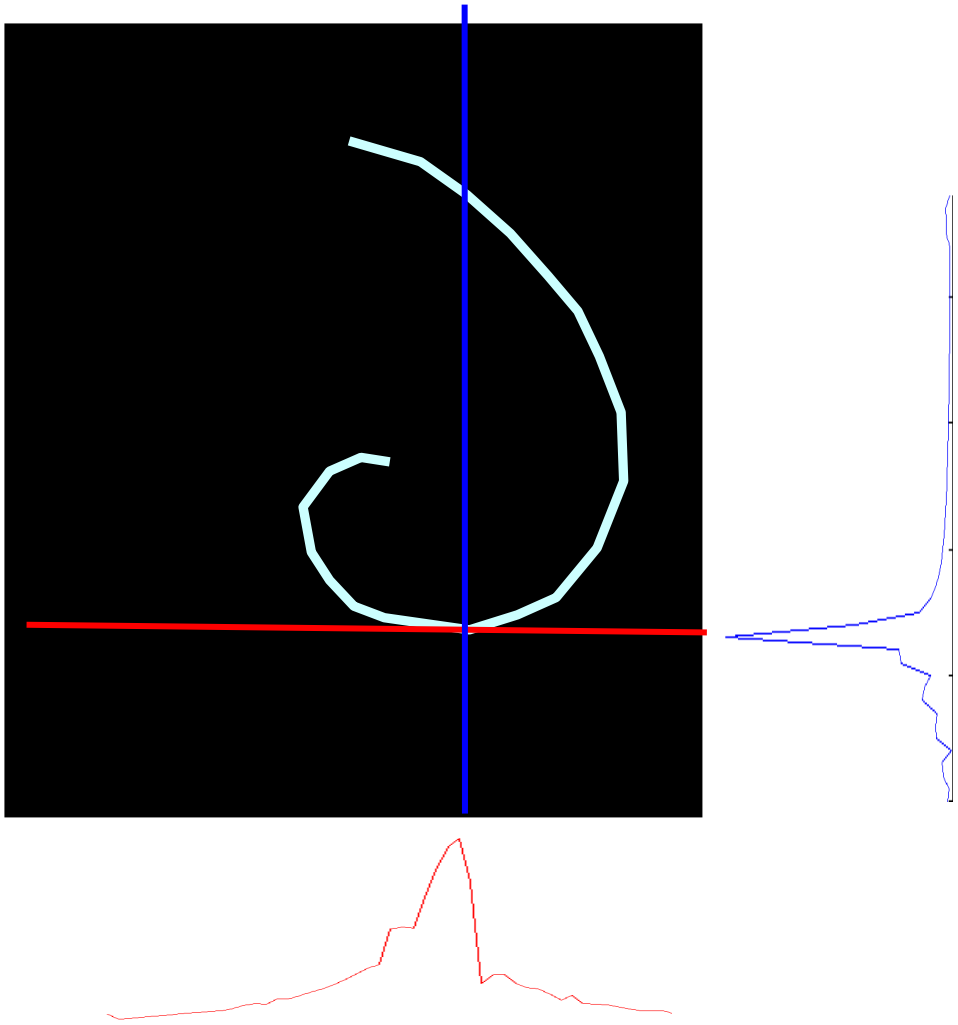

Figure 7.3 – This figure shows the signal profiles as indicated:
red (left): profile along the line tangential to the signal trajectory
blue (right): profile of excitation perpendicular to the trajectory from the double echo version of SWIRLY

the centroid, which is somewhat akin to the determination of the resolution along the time-encoded dimension in sequences such as RASER. Each profile should be considered separately.

The movement of the wave, or line, of excitation tangential to the trajectory can be represented as two components, the tangential velocity driving the centroid along the trajectory and the rotational velocity of the line about the centroid. The perpendicular profile will arise from a combination of the angular velocity imparted by the gradients and the centrifugal velocity generated by the frequency sweep. The excitation at the centroid will be dependant only upon the tangential velocity, while the excitation at every other point along that line will be dictated by both the tangential velocity and rotational velocity of the line of excitation about the certroid. Thus, the excitation of any point on the tangential line will be proportional to its distance from the centroid. As the line of excitation travels along the defined trajectory, those isochromats falling within the excitation line at a point nearer the centroid will have lower instantaneous velocity and experience more RF energy and subsequently contribute proportionally more signal during acquisition than those isochromats in the excitation wave further from the centroid. The profile along the tangential line of excitation calculated from Bloch simulation is shown in Figure 7.3 in red.

Now, consider the profile of excitation of the wave perpendicular to the trajectory. Conversion to polar-coordinate space conveniently shows SWIRLY as a frequency sweep with a constant gradient, revealing that the perpendicular profile will resemble that of a frequency swept pulse without time encoding, dependent primarily on the sweep rate.

This profile is the narrowest. The profile of excitation perpendicular to the trajectory is shown in Figure 7.3 in blue.

The profiles in Figure 7.3 show that while the maximum signal is well localized to the expected trajectory, because the acquired signal is a summation over whole spatial domain, the contributions from other regions, while contributing proportionally much less signal, contribute substantially to the collected signal when summed, suggesting that a geometric assignment of signal is an insufficient method of reconstruction and another method should be considered. This insufficiency is better illuminated using Bloch simulations with two spatial dimensions.

B_1 and B_0 inhomogeneity compensation

The inherently spatial nature of SWIRLY makes it well suited to B_1 and B_0 inhomogeneity compensation. The modulation of gradients, RF amplitude, and RF frequency allows many degrees of freedom for compensation. By mapping the B_1 inhomogeneity and knowing the trajectory of the region of resonance, the RF amplitude can be modulated to compensate by simply increasing the amplitude proportionally when the resonance region is in an area of low signal. Similarly a B_0 map and known trajectory can be used for compensation for main magnetic field variations. The RF frequency and gradients can be modulated to follow the desired trajectory in the presence of the B_0 inhomogeneities. The capacity to independently adjust for the main magnetic field and RF field actually experienced by each resonance region gives this compensation method particular flexibility and robustness in the spatial domain.

7.3 Methods

Simulation

Simulations were performed with a program based on the Bloch equations using a combination of Matlab and C. Results from these simulations can be used to show the sequential excitation along a trajectory in the rapid-passage, linear region (86). The full-trajectory z-axis magnetization pattern in Figure 7.2b was created using a half chirp pulse and sinusoidal gradients to produce an Archimedean spiral with parameters Tp = 20 ms, b_W = 27.5 kHz, and field of view (FOV) of 51 x 51. This Figure shows a narrow ridge with relatively consistent amplitude. Simulations can also be used to predict the behavior of the sequence in acquisition. In the case of SWIRLY, to replicate the experimental acquisition the signal must be summed over the whole space for the duration of the acquisition. As with the experiment, data collected for each of the rotated spirals can be combined to form an image. Figure 7.4a shows a simulated 2D object consisting of three small circles and one large circle, all with uniform signal intensity. Figure 7.4b shows the data acquired from simulation displayed such that along the horizontal axis is the time-dependant acquisition and the vertical axis is a series of separate spirals ordered according to rotation about the through-plane axis, together forming a spirogram. Figures 7.4c and d are the reconstructed data using geometric and inverse problem methods respectively, which clearly confirms the aforementioned invalidity of assuming the signal is sufficiently close to a delta function and the consequent inadequacy of geometric reconstruction. The simulation data for Figure 7.4 was generated with simulation parameters $b_{W,excitation}$ = 40 kHz, $b_{W,acquistion}$ = 80 kHz, Tp = at = 6.0 ms, TE = 21 ms, and since each spiral was simulated separately with no memory of the previous spirals, the

TR can be considered infinite. The trajectory is an Archimedean spiral traversed with constant angular velocity. The exception to these parameters is that to maintain the same flip-angle in spite of the gaps, the SWIRLY SWIFT pulse would need to be run with the RF amplitude or pulse duration increased proportional to 1/dc, the latter chosen here, imparting a smaller band-width. Beyond validation of expectation and experimental results, the predictive power of simulations is of particular importance in reconstruction for the generation of the transfer function for the inverse problem solution, which will be described and discussed later.

Experimental

A 4 T magnet having a 90 cm bore diameter (Oxford Magnet Technology, Oxfordshire, UK) was used with a clinical gradient system (Sonata, Siemens, Erlangen, Germany) and an imaging spectrometer console (Unity Inova, Varian, Palo Alto, CA) for all experiments. The RF coil employed in both transmit and receive is a quadrature surface coil consisting of two loops. In all experiments, one 50 mL test tube and three 10 mL test tubes were positioned upright in the coil, and the images were collected in the coronal plane. SWIRLY experimental results were collected using a double-echo sequence with inversion pulses from the hyperbolic secant family. The experiments were performed with $b_{W,excitation}$ = 40 kHz, $b_{W,acquistion}$ = 80 kHz Tp = at = 6.4 ms, TE = 21 ms, and TR = 4 s. The pulse powers were calibrated by arraying the pulse width. The FOV has a diameter of 20 cm. The number of complex points along the trajectory was 512, and the number of rotated spirals collected was 128, following an Archimedean spiral trajectory with constant angular velocity.

Reconstruction

Clearly the typical Fourier transform reconstruction employed by the vast majority of MR imaging methods is inappropriate for this sequence. Further, geometric reconstruction cannot be done, assigning signal along the trajectory according to the known spatial-temporal relationship, which has been used along one dimension with previous time-encoding sequences. Because the excitation profile is not sufficiently close to a delta function, a geometric method is too simplistic, as can be demonstrated in both simulation and experiment (Figure 7.4 c,g). The similarity between the simulation data and the experiment data strongly suggests the potential for using an inverse mapping problem to generate a more accurate image by calculating the least-squares solution. The general form of the inverse mapping problem comes from earlier literature (87,88). This reconstruction method has been employed with other imaging modalities, such as electrocardiography (89). Inverse mapping has been used in MRI for data collected using standard encoding, which is useful for addressing Gibb's ringing, but time and computational demands favor Fourier methods in the vast majority of circumstances (90,91). Similar methods have been applied in MRI along one dimension for enhanced resolution (12,76,92).

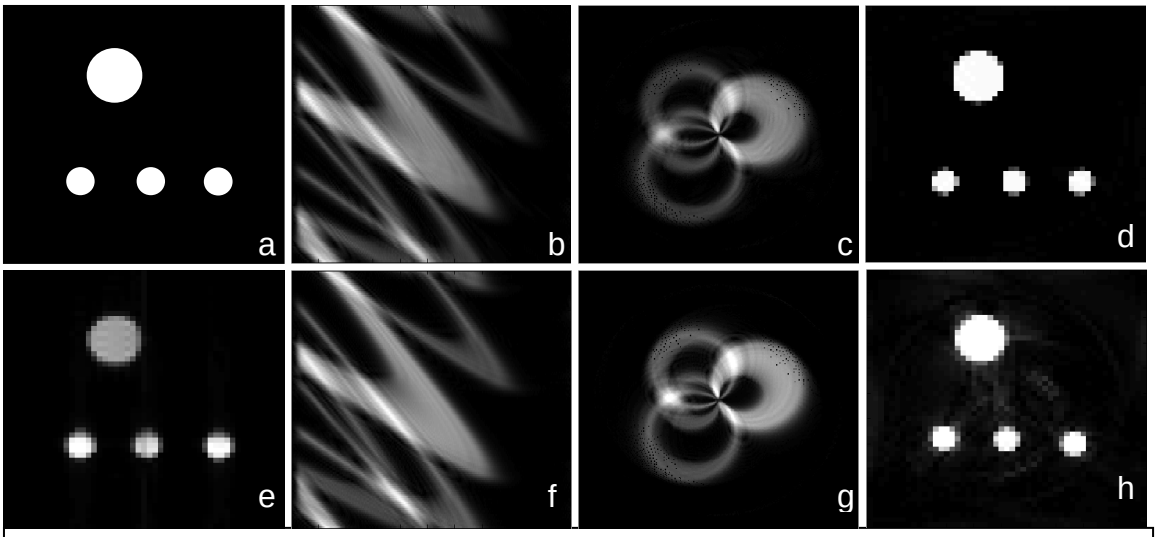

Figure 7.4 – This figure shows a simulated and real object (a and e respectively). The resulting spirogram when acquired with SWIRLY is shown in (b) and (f). If a simple geometric assignment is used for reconstruction, figures (c) and (g) are produced. However, when an inverse problem solution is used, the resulting simulated images is shown in (d) and the resulting experimental image is shown in (h).

The generation and implementation of the inverse problem solution for SWIRLY is displayed graphically in Figure 7.5 where H is the transfer matrix and H^{+} is the pseudoinverse of that matrix. Worth mentioning is the fact that SWIRLY reconstruction involves four-dimensions, x y, time, and rotation. Being that inverting a two-dimensional matrix is a better understood and more frequently addressed problem, the four dimensions were condensed into two dimensions, treating x and y as one dimension, the range space, and time and rotation as the other, the domain space. The aforementioned Bloch simulation program was used to approximate the forward problem and thereby obtain an estimate of H. A program was written for calculating a pseudoinverse which employed singular value decomposition (SVD), regularization, and other functions available in Matlab or as a part of the Matlab package Regularization Tools (93). The

condition number of the transfer function applied to the shown images is 17.8, in other words, the matrix is well conditioned. Applying the resulting solution to experimental data reliably produced images of the phantom both in simulation and experiment. For Figures 7.4d and h, H is the same. Further, the same matrix can be used for any simulated or experimental data collected with the same parameters. From Figure 7.4, improvements using the inverse problem solution for reconstruction rather than a geometric solution are abundantly clear in both simulation and experiment.

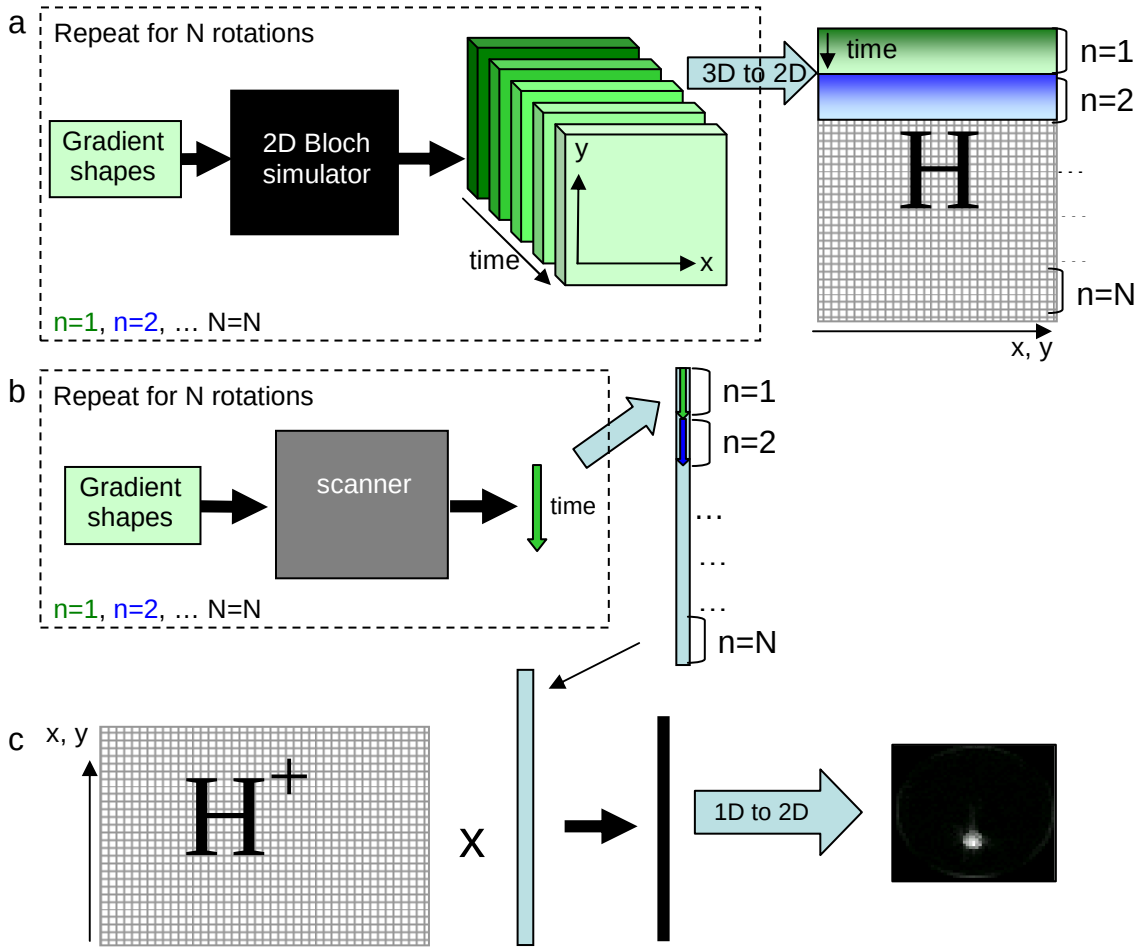

Figure 7.5 – Schematic diagram of the inverse problem reconstruction. The forward problem is shown in (a). The experimental acquisition is shown in (b). Finally the inverse problem reconstruction is shown in (c).

7.4 Results

SWIRLY

The experiment with four tubes in cross-section, three small and one large, is shown as reconstructed by using an inverse problem solution on the left-hand side of Figure 7.6. The right-hand side is a gradient echo scout image. Both SWIRLY and GRE images are shown with 51 x 51 resolution. The image shows minimal artifacts.

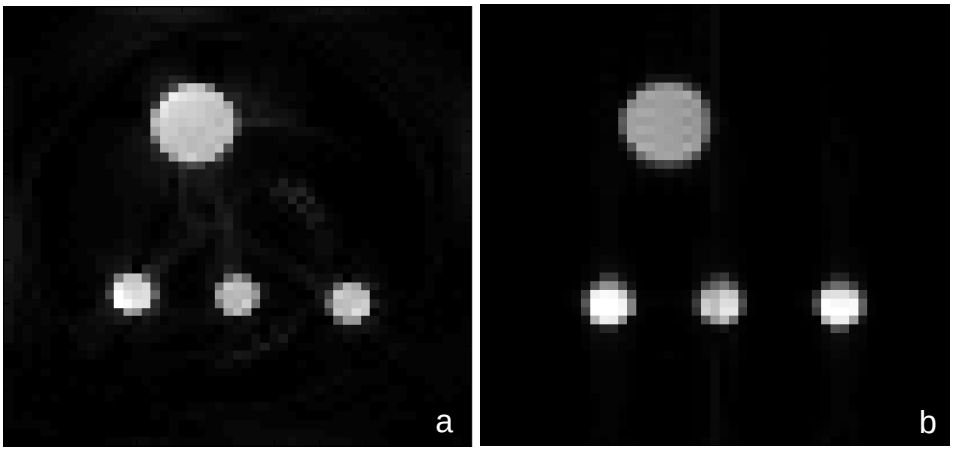

Figure 7.6 – On the left (a) is an experimental image acquired at 4 T with a double echo SWIRLY sequence and reconstructed with an inverse problem solution. The figure on the right (b) is a GRE scout of the object collected at a comparable resolution.

SWIRLY SWIFT

A SWIRLY SWIFT experiment was simulated, and the results are shown in Figure 7.7. The double echo SWIRLY results reconstructed with an inverse problem method are shown in Figure 7.7a. A gradient echo scout image is shown in Figure 7.8b for comparison. A duty cycle of 50% was used with 16-times over-sampling, meaning that in the file that describes the RF shape 16 points were used to describe each cycle. The artifacts incurred with this imaging method were negligible such that the window and level of the image were substantially narrowed and lowered to show any differences from the 2D simulated signal intensity map.

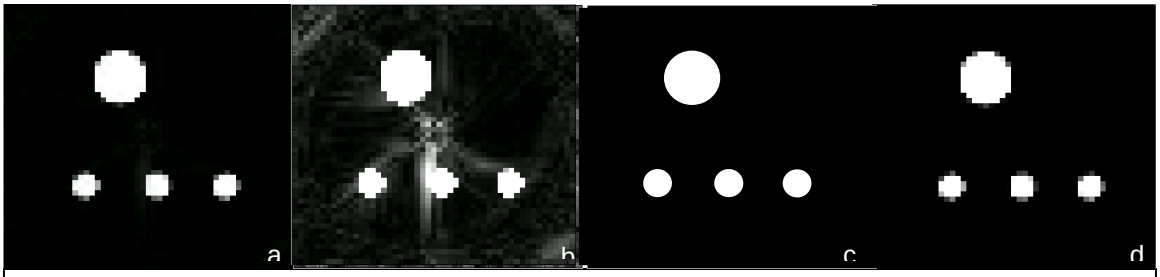

Figure 7.7 – SWIRLY SWIFT simulation. Figure (a) shows an image acquired in simulation with SWIRLY SWIFT. Figure (b) shows the same image as a but with the noise scaled up ten times in order to show the artifacts. Figure (c) is the simulated object displayed with high resolution, and Figure (d) shows the simulated object scaled to the acquired resolution of 51 x 51.

B_1 and B_0 Inhomogeneity Compensation

To demonstrate the flexibility of SWIRLY to compensate for B_1 inhomogeneities a two-dimensional inhomogeneity pattern shown in Figure 7.8c was applied during simulations. The inhomogeneity pattern was chosen to resemble the field generated by a pair of loop coils in quadrature, in this case a coil designed for breast imaging. A simulated phantom was chosen to look like the phantom used for testing the breast imaging coil. The phantom can be seen in Figure 7.8a with the approximate position of the loops. Figure 7.8b shows the simulated phantom. The double-echo version of SWIRLY was chosen to capitalize on the robustness of the adiabatic HSn pulses despite the field inhomogeneities. The result of applying the inhomogeneity is shown in Figure 7.8d. A 51 x 51 resolution was used. Given a map of the B_1 inhomogeneity, new RF shapes were generated for each of the spirals, which were designed to compensate for the B_1 inhomogeneity during the actual experiment. These new RF shapes were used to generate the image shown in 7.8e. Similarly, SWIRY is also capable of addressing B_0 inhomogeneities. The theory is described in detail for 1D time encoding by Tal and Frydman (19) and can be extended to

SWIRLY using methods much like those used for the B_1 compensation. Should compensating for either B_1 or B_0 during the experiment be undesirable or unfeasible for some reason, the inverse problem can easily be used to compensate in post-processing. This method also requires some prior knowledge about the RF profile or static magnetic field, meaning that a map of the inhomogeneities is needed. Applying the map to the simulation when generating the transfer matrix will then create a matrix that compensates for the inhomogeneity.

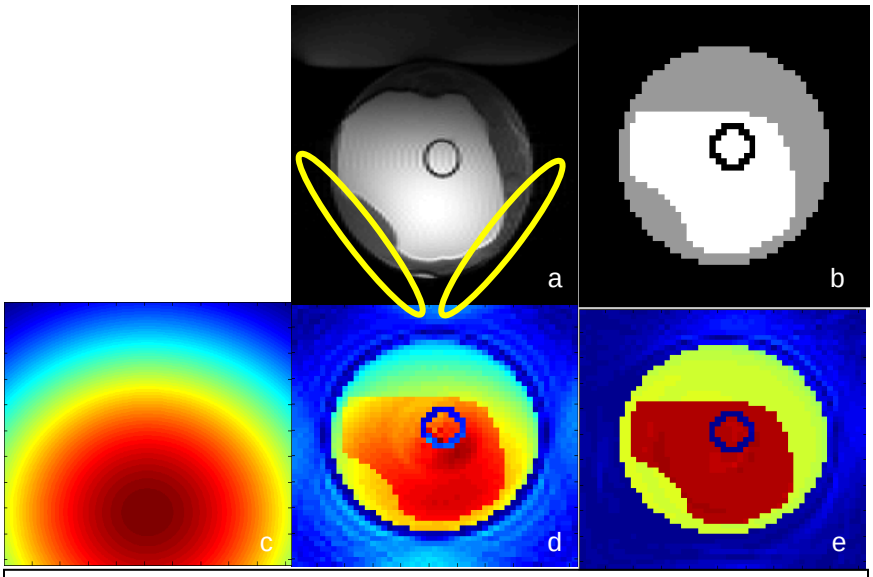

Figure 7.8 – Inhomogeneity compensation demonstration. The image of a phantom with coil position (a) and simulated phantom (b) are given for reference. The B_1 inhomogeneity is shown in (c) and the image without compensation is shown in (d). The image with inhomogeneity compensation is shown in (e).

7.5 Discussion

As the newest member of the spatiotemporal-encoded family, SWIRLY has the special advantage of being able to treat regions of resonance independently not only during receive but during excitation as well. This property gives SWIRLY particular advantages over sequences with one or more dimensions of frequency or phase encoding as well as advantages over other entirely spatially encoded sequences that lack independence in their excitation scheme. The extra degrees of freedom allowed with spatially independent excitation make SWIRLY better suited to compensate for multi-dimensional field non-uniformities.

The use of the inverse problem solution with spatially encoded data is of tremendous benefit, arguably necessary. This method of reconstruction does demand more time and computational power. However, these demands can be significantly reduced by building a library of transfer functions ready to be applied to data sets generated with the same parameters. With such a library, inverse problem reconstruction would be only slightly longer than Fourier reconstruction.

In Fourier transformed imaging, spatial resolution is determined by the acquisition parameters, whereas the resolution in spatiotemporal imaging is derived from the excitation. Consequently, maintaining reasonable excitation times and amplitudes can limit the achievable pixel size for time encoding, However, Ben-Eliezer et al. recently showed that they were able to recover this resolution in hybrid sequences with super resolution (SR) techniques (12). The SR reconstruction is in fact a 1D inverse problem solution applied along the spatiotemporal encoding direction. This technique expanded to two dimensions is equivalent to simply increasing the number of pixels along the x and y

coordinates of the simulation used to generate the transfer function. Unfortunately, the expansion to two spatial dimensions makes for an unwieldy matrix, the inversion of which is a formidable computational request. However, a combination of iterative inversion methods and advanced computing systems are being explored as these resolution gains could substantially enhance SWIRLY's imaging capabilities. Entirely spatiotemporal sequences with grid-like excitation seem to have potential to greatly benefit from the implementation of inverse problem methods. Like SWIRLY they would need to combine x and y axes into one dimension of the transfer matrix, with spatiotemporal encoding along the other dimension.

Modulating a frequency swept pulse and simultaneously applying shaped gradients, a trajectory in the spatial domain can be carefully defined. This alternative multi-dimensional control in the spatial domain offers significant advantages in compensating for B_1 and B_0 inhomogeneities. Using a B_1 and B_0 maps, the RF amplitude and frequency sweep can be modulated to address non-uniformities. This will increase the flip angle in regions with low B_1 to produce a more homogeneous image while maintaining sufficiently low SAR values, which is of particular importance for ultra-high magnetic field applications, and it will shift the phase back into it's appropriate position in space, removing distortions. The capacity to treat these problems from an entirely spatial perspective should have novel benefits when used alone or in combination with existing methods. For B_1 inhomogeneities, compensating during the experiment will be better for recovering more signal. However, should a situation arise that compensation could not be done during the experiment, compensating in the post processing is a very reasonable option. Conveniently, the field maps needed for the post processing will already have

been acquired for the experimental method. Using the two methods together or in concert with other shimming methods is also possible and is being further explored.

In addition to the gradient echo and spin echo versions of SWIRLY shown here, SWIRLY can also be implemented with a sweep imaging with Fourier transform (SWIFT) acquisition method (80-85). An excitation pattern similar to the other implementations could be used expect with the introduction of gaps in the RF pulse during which time signal may be acquired for nearly simultaneous transmit and receive, bringing many of the unique and valuable properties of SWIFT into an entirely spatial domain (80-85).

Chapter 8: Conclusion

The research presented here reveals much opportunity for future work and gives direction for determining the most beneficial applications. Though 7 T imaging of the liver and uterus is not yet ready for clinical implementation, there are a number of interesting and important scientific research applications to explore. Ultimately the goals are to develop diagnostic methods, treatment monitoring protocols, and a closer understanding of particular diseases. The study of disease states from a research perspective must precede clinical applications, and the study of normal tissue characteristics must precede disease research. The instabilities and inhomogeneities at 7 T make it currently inappropriate as a diagnostic tool, but improvements in B_1^+ shimming and effective use of parallel imaging make feasible the imaging of select patient volunteers for research purposes. In both the liver and uterus, imaging of cancers at high fields would be a valuable step forward. Particular advantages are expected in understanding the potential diagnostic role of new contrast mechanisms like $T_{1\rho}$ and $T_{2\rho}$ especially as captured by RAFF. Likewise, the previously demonstrated value of cancer spectroscopy stands to gain much from the increased spectral dispersion. In addition to small-scale patient studies, the current level of moderate consistency would be tolerable for somewhat more substantial studies of normal volunteers. Determining what factors in fertility can be detected with both new and improved contrast mechanisms would be of particular interest. Because of the dynamic nature of the endometrium, this would necessarily involve several carefully-timed scans for each volunteer, and volunteers would need to be recruited from three categories: unknown fertility, known fertility, and those undergoing fertility treatments.

SWIRY has a promising future and many avenues to follow. Improvements can be made in speed, efficiency, resolution, and 3D capabilities. Further development of inhomogeneity compensation is of much interest. Moreover, SWIRLY taken to higher field strengths could more dramatically put to use this compensation. SWIRLY SWIFT presents even more opportunities. With SWIRLY's capacity to compensate for inhomogeneities and SWIFT's sensitivity to short T_2 signal there is tremendous potential to approach the complex problem of not only imaging bone, but of imaging bone with metal implants, something thought impossible for MR in the past and still a substantial challenge for other imaging modalities. SWIRLY is a unique and valuable addition to MR with great potential for advancing research in its field.

Chapter 9: References

1. Bloembergen N. PEMPRV. Relaxation effects in nuclear magnetic resonance absorption. Physical Review 1948;73:679-712.
2. Bloch F. Nuclear Induction. Physical Review 1946;70:460-474.
3. Chmurny GNaH, D. I. The Ancient and Honourable Art of Shimming. Concepts in Magnetic Resonance 1990;2:131-149.
4. Hutchinson GJaJMS. An NMR imaging data acquisition system. J Phys E: Sci Instrum 1981;14(10):1131-1132.
5. Bolinger L. Magnetic Resonance Imaging. University of Iowa; 2002. p 1-53.
6. Haacke EM BR, Thompson MR, Venkatesan R. Magnetic Resonance Imaging: Physical Principles and Sequence Design: Wiley-Liss; 1999.
7. Garwood M, DelaBarre L. The return of the frequency sweep: designing adiabatic pulses for contemporary NMR. J Magn Reson 2001;153(2):155-177.
8. Lauterbur PC. Image Formation by Induced Local Interactions: Examples Employing Nuclear Magnetic Resonance. Nature 1973;242:190-191.
9. Mansfield P. Multi-planar image formation using NMR spin echoes. J Phys C: Solid State Phys 1977;10:L55-L58.
10. Chamberlain R, Park JY, Corum C, Yacoub E, Ugurbil K, Jack CR, Jr., Garwood M. RASER: a new ultrafast magnetic resonance imaging method. Magn Reson Med 2007;58(4):794-799.
11. Ben-Eliezer N, Frydman L. Spatiotemporal encoding as a robust basis for fast three-dimensional in vivo MRI. NMR Biomed 2011.
12. Ben-Eliezer N, Irani M, Frydman L. Super-resolved spatially encoded single-scan 2D MRI. Magn Reson Med 2010;63(6):1594-1600.
13. Ben-Eliezer N, Shrot Y, Frydman L. High-definition, single-scan 2D MRI in inhomogeneous fields using spatial encoding methods. Magn Reson Imaging 2010;28(1):77-86.
14. Frydman L, Scherf T, Lupulescu A. The acquisition of multidimensional NMR spectra within a single scan. Proc Natl Acad Sci U S A 2002;99(25):15858-15862.
15. Shapira B, Frydman L. Spatially encoded pulse sequences for the acquisition of high resolution NMR spectra in inhomogeneous fields. J Magn Reson 2006;182(1):12-21.
16. Shrot Y, Frydman L. Spatially encoded NMR and the acquisition of 2D magnetic resonance images within a single scan. J Magn Reson 2005;172(2):179-190.
17. Shrot Y, Frydman L. Single-scan NMR spectroscopy at arbitrary dimensions. J Am Chem Soc 2003;125(37):11385-11396.
18. Shrot Y, Tal A, Frydman L. New developments in the spatial encoding of spin interactions for single-scan 2D NMR. Magn Reson Chem 2009;47(5):415-422.
19. Tal A, Frydman L. Spatial encoding and the single-scan acquisition of high definition MR images in inhomogeneous fields. J Magn Reson 2006;182(2):179-194.
20. Tal A, Frydman L. Single-scan multidimensional magnetic resonance. Prog Nucl Magn Reson Spectrosc 2010;57(3):241-292.

21. Tal A, Frydman L. Spectroscopic imaging from spatially-encoded single-scan multidimensional MRI data. J Magn Reson 2007;189(1):46-58.
22. Ugurbil K, Adriany G, Andersen P, Chen W, Garwood M, Gruetter R, Henry PG, Kim SG, Lieu H, Tkac I, Vaughan T, Van De Moortele PF, Yacoub E, Zhu XH. Ultrahigh field magnetic resonance imaging and spectroscopy. Magn Reson Imaging 2003;21(10):1263-1281.
23. Schick F. Whole-body MRI at high field: technical limits and clinical potential. European Radiology 2005;15(5):946-959.
24. Vaughan JT, Garwood M, Collins CM, Liu W, DelaBarre L, Adriany G, Andersen P, Merkle H, Goebel R, Smith MB, Ugurbil K. 7T vs. 4T: RF power, homogeneity, and signal-to-noise comparison in head images. Magn Reson Med 2001;46(1):24-30.
25. Bolan PJ, Adriany G, Akgun C, Andersen P, Auerbach E, Delabarre L, Goerke U, Gozubuyuk A MG, Moeller S, Styczynski Snyder AL, Snyder CJ, Strupp J, Tian J, Van, de Moortele P-F VJ, Ugurbil K. Technical Aspects of Ultra-High Field (7 Telsa) Body MR Imaging and Spectroscopy. 2007; Chicago.
26. Metzger GJ, Snyder C, Akgun C, Vaughan T, Ugurbil K, Van de Moortele PF. Local B1+ shimming for prostate imaging with transceiver arrays at 7T based on subject-dependent transmit phase measurements. Magn Reson Med 2008;59(2):396-409.
27. Wiesinger F, Van de Moortele PF, Adriany G, De Zanche N, Ugurbil K, Pruessmann KP. Parallel imaging performance as a function of field strength--an experimental investigation using electrodynamic scaling. Magn Reson Med 2004;52(5):953-964.
28. Ohliger MA, Grant AK, Sodickson DK. Ultimate intrinsic signal-to-noise ratio for parallel MRI: electromagnetic field considerations. Magn Reson Med 2003;50(5):1018-1030.
29. Yacoub E, Harel N, Ugurbil K. High-field fMRI unveils orientation columns in humans. Proc Natl Acad Sci U S A 2008;105(30):10607-10612.
30. Yacoub E, Shmuel A, Logothetis N, Ugurbil K. Robust detection of ocular dominance columns in humans using Hahn Spin Echo BOLD functional MRI at 7 Tesla. Neuroimage 2007;37(4):1161-1177.
31. Yacoub E, Van De Moortele PF, Shmuel A, Ugurbil K. Signal and noise characteristics of Hahn SE and GE BOLD fMRI at 7 T in humans. Neuroimage 2005;24(3):738-750.
32. Yacoub E, Duong TQ, Van De Moortele PF, Lindquist M, Adriany G, Kim SG, Ugurbil K, Hu X. Spin-echo fMRI in humans using high spatial resolutions and high magnetic fields. Magn Reson Med 2003;49(4):655-664.
33. Yao B, Li TQ, Gelderen P, Shmueli K, de Zwart JA, Duyn JH. Susceptibility contrast in high field MRI of human brain as a function of tissue iron content. Neuroimage 2009;44(4):1259-1266.
34. Duyn JH, van Gelderen P, Li TQ, de Zwart JA, Koretsky AP, Fukunaga M. High-field MRI of brain cortical substructure based on signal phase. Proc Natl Acad Sci U S A 2007;104(28):11796-11801.

35. Burgess RE, Yu Y, Christoforidis GA, Bourekas EC, Chakeres DW, Spigos D, Kangarlu A, Abduljalil AM, Robitaille PM. Human leptomeningeal and cortical vascular anatomy of the cerebral cortex at 8 Tesla. J Comput Assist Tomogr 1999;23(6):850-856.
36. Vaughan T, DelaBarre L, Snyder C, Tian J, Akgun C, Shrivastava D, Liu W, Olson C, Adriany G, Strupp J, Andersen P, Gopinath A, van de Moortele PF, Garwood M, Ugurbil K. 9.4T human MRI: preliminary results. Magn Reson Med 2006;56(6):1274-1282.
37. Vaughan JT, Adriany G, Snyder CJ, Tian J, Thiel T, Bolinger L, Liu H, DelaBarre L, Ugurbil K. Efficient high-frequency body coil for high-field MRI. Magn Reson Med 2004;52(4):851-859.
38. Vaughan JT, Snyder CJ, DelaBarre L, Tian J, Adriany G, Anderson P, Strupp J, Ugurbil K. Clinical Imaging at 7T with a 16 Channel Whole Body Coil and 32 Receive Channels. 2009; Honolulu. p 391.
39. Snyder C DL, Van de Moortele P-F, Styczynski Snyder A, Akgun C, Tian J, Metzger G, Ugurbil K, Vaughan J. Stripline/TEM Transceiver Array for 7T Body Imaging. 2007; Berlin. p 164.
40. Orzada S, Maderwald S, Oehmigen M, Ladd M, Solbach K, Bitz A. An 8-Channel TX, 16-Channel Flexible Body Coil at 7 Tesla Using Both Branches of Centrally Fed Strip Lines as Individual Receive Elements. 2010; Stockholm. p 641.
41. Adriany G, Van de Moortele PF, Wiesinger F, Moeller S, Strupp JP, Andersen P, Snyder C, Zhang X, Chen W, Pruessmann KP, Boesiger P, Vaughan T, Ugurbil K. Transmit and receive transmission line arrays for 7 Tesla parallel imaging. Magn Reson Med 2005;53(2):434-445.
42. Orzada S MS, Poser BA, Johst S, Kannengiesser S, Ladd ME, Bitz AK. Time-interleaved acquisition of modes: An analysis of SAR and image contrast implications. MRM 2011;In Press.
43. Wiesinger F, Van de Moortele PF, Adriany G, De Zanche N, Ugurbil K, Pruessmann KP. Potential and feasibility of parallel MRI at high field. NMR Biomed 2006;19(3):368-378.
44. Snyder CJ, DelaBarre L, Moeller S, Tian J, Akgun C, Van De Moortele P-F, Bolan PJ, Ugurbil K, Vaughan JT, Metzger GJ. Comparison Between Eight- and Sixteen-Channel TEM Transceive Arrays for Body Imaging at 7 Tesla. Magnetic Resonance in Medicine 2011.
45. Van de Moortele PF, Akgun C, Adriany G, Moeller S, Ritter J, Collins CM, Smith MB, Vaughan JT, Ugurbil K. B(1) destructive interferences and spatial phase patterns at 7 T with a head transceiver array coil. Magn Reson Med 2005;54(6):1503-1518.
46. Orzada S MS, Oehmigen M, Ladd M, Solbach K, Bitz A. An 8-Channel TX, 16-Channel Flexible Body Coil at 7 Tesla Using Both Branches of Centrally Fed Strip Lines as Individual Receive Elements. 2010; Stockholm.
47. Orzada S, Maderwald S, Poser BA, Bitz AK, Quick HH, Ladd ME. RF excitation using time interleaved acquisition of modes (TIAMO) to address B1 inhomogeneity in high-field MRI. Magn Reson Med 2010;64(2):327-333.

48. Snyder CJ, DelaBarre L, Metzger GJ, van de Moortele PF, Akgun C, Ugurbil K, Vaughan JT. Initial results of cardiac imaging at 7 Tesla. Magn Reson Med 2009;61(3):517-524.
49. van Elderen SG, Versluis MJ, Webb AG, Westenberg JJ, Doornbos J, Smith NB, de Roos A, Stuber M. Initial results on in vivo human coronary MR angiography at 7 T. Magnetic Resonance in Medicine 2009;62(6):1379-1384.
50. DelaBarre L. 2011.
51. Delabarre LJ WP, Snyder CJ, van de Moortele P-F, Metzger GJ, Zuehlsdorff S, Nielles-, Vallespin S BP, Auerbach E, Ugurbil K, Jerecic R, Vaughan JT. Cardiac Cine: Advances at 7T. 2009; Honolulu.
52. Suttie JJ, Delabarre L, Pitcher A, van de Moortele PF, Dass S, Snyder CJ, Francis JM, Metzger GJ, Weale P, Ugurbil K, Neubauer S, Robson M, Vaughan T. 7 Tesla (T) human cardiovascular magnetic resonance imaging using FLASH and SSFP to assess cardiac function: validation against 1.5 T and 3 T. NMR Biomed 2010.
53. Styczynski Snyder AL, Snyder CJ, DelaBarre L, Van de Moortele P-F, Vaughan JT, Ugurbil K, Garwood M, Bolan PJ. Preliminary Experience with Liver MRI and 1H MRS at 7 tesla. 2007; Berlin. p 729.
54. Styczynski Snyder AL, Moeller S, Garwood M, Bolan PJ. Parallel Imaging in the Human Liver at 7 Tesla. 2008; Toronto.
55. Hezel F KP, Thalhammer C, Özerdem C, Renz W, Niendorf T. Initial Results of Abdominal MRI at 7T Using a 16 channel Transmit/Receive Coil. 2011.
56. Styczynski Snyder AL, Snyder CJ, DelaBarre LJ, Van De Moortele PF, Haddadin IS, Truskinovsky A, Vaughan JT, Ugurbil K, Garwood M, Michaeli S. Endometrial Imaging at High Magnetic Fields: Feasibility of In-Vivo Studies at 7 T. 2007; Berlin. p 573.
57. Styczynski Snyder AL, Liimatainen T, Goerke U, Garwood M, Michaeli S. Exploring Alternative Contrast in the Uterus at High Magnetic Fields. 2008; Toronto.
58. Metzger G SJ, Bi X, Weale P, Zuehlsdorff S, Auerbach E, Ugurbil K, Van de Moortele P-F. Initial Experience with Non-Contrast Enhanced Renal Angiography at 7.0 Tesla. 2010; Stockholm. p 401.
59. Ramalho M, Altun E, Heredia V, Zapparoli M, Semelka R. Liver MR imaging: 1.5T versus 3T. Magn Reson Imaging Clin N Am 2007;15(3):321-347, vi.
60. Li CW, Kuo YC, Chen CY, Kuo YT, Chiu YY, She FO, Liu GC. Quantification of choline compounds in human hepatic tumors by proton MR spectroscopy at 3 T. Magn Reson Med 2005;53(4):770-776.
61. Gruetter R, Weisdorf SA, Rajanayagan V, Terpstra M, Merkle H, Truwit CL, Garwood M, Nyberg SL, Ugurbil K. Resolution improvements in in vivo 1H NMR spectra with increased magnetic field strength. J Magn Reson 1998;135(1):260-264.
62. Mountford CE, Doran S, Lean CL, Russell P. Proton MRS can determine the pathology of human cancers with a high level of accuracy. Chem Rev 2004;104(8):3677-3704.

63. Ramirez de Molina A, Banez-Coronel M, Gutierrez R, Rodriguez-Gonzalez A, Olmeda D, Megias D, Lacal JC. Choline kinase activation is a critical requirement for the proliferation of primary human mammary epithelial cells and breast tumor progression. Cancer Res 2004;64(18):6732-6739.
64. Meisamy S, Bolan PJ, Baker EH, Bliss RL, Gulbahce E, Everson LI, Nelson MT, Emory TH, Tuttle TM, Yee D, Garwood M. Neoadjuvant chemotherapy of locally advanced breast cancer: predicting response with in vivo (1)H MR spectroscopy--a pilot study at 4 T. Radiology 2004;233(2):424-431.
65. Bell JD, Bhakoo KK. Metabolic changes underlying 31P MR spectral alterations in human hepatic tumours. NMR Biomed 1998;11(7):354-359.
66. Kuo YT, Li CW, Chen CY, Jao J, Wu DK, Liu GC. In vivo proton magnetic resonance spectroscopy of large focal hepatic lesions and metabolite change of hepatocellular carcinoma before and after transcatheter arterial chemoembolization using 3.0-T MR scanner. J Magn Reson Imaging 2004;19(5):598-604.
67. Katz-Brull R, Rofsky NM, Lenkinski RE. Breathhold abdominal and thoracic proton MR spectroscopy at 3T. Magn Reson Med 2003;50(3):461-467.
68. Griswold MA JP, Heidemann RM, Nittka M, Jellus V, Wang J, Berthold Kiefer B, Haase A. Generalized autocalibrating partially parallel acquisitions (GRAPPA). Magnetic Resonance in Medicine 2002;47(6):1202-1210.
69. Liimatainen T, Sorce DJ, O'Connell R, Garwood M, Michaeli S. MRI contrast from relaxation along a fictitious field (RAFF). Magn Reson Med 2010;64(4):983-994.
70. Michaeli S, Oz G, Sorce DJ, Garwood M, Ugurbil K, Majestic S, Tuite P. Assessment of brain iron and neuronal integrity in patients with Parkinson's disease using novel MRI contrasts. Mov Disord 2007;22(3):334-340.
71. Frei KA, Kinkel K. Staging endometrial cancer: role of magnetic resonance imaging. J Magn Reson Imaging 2001;13(6):850-855.
72. Saez F, Urresola A, Larena JA, Martin JI, Pijuan JI, Schneider J, Ibanez E. Endometrial carcinoma: assessment of myometrial invasion with plain and gadolinium-enhanced MR imaging. J Magn Reson Imaging 2000;12(3):460-466.
73. Pipe JG. Spatial encoding and reconstruction in MRI with quadratic phase profiles. Magn Reson Med 1995;33(1):24-33.
74. Pipe JG. Analysis of localized quadratic encoding and reconstruction. Magn Reson Med 1996;36(1):137-146.
75. Meyerand ME, Wong EC. A time encoding method for single-shot imaging. Magn Reson Med 1995;34(4):618-622.
76. Shen J, Xiang Y. High fidelity magnetic resonance imaging by frequency sweep encoding and Fourier decoding. J Magn Reson 2010;204(2):200-207.
77. Powell N J MM, Valette J, Henry P-G, Garwood M. A New Method for Single-shot 2-D OVS. 2008.
78. Conolly S, Glover G, Nishimura D, Macovski A. A reduced power selective adiabatic spin-echo pulse sequence. Magn Reson Med 1991;18(1):28-38.
79. Silver MS JR, Hoult DI. Highly selective $\pi/2$ and π pulse generation. J Magn Reson 1984;59:347-351.

80. Corum CA, Moeller S, Idiyatullin D, Garwood M. Signal processing and image reconstruction for SWIFT. 2007; Berlin. p 1669.
81. Corum CA ID, Moeller S, Garwood M. Progress in 3D Imaging at 4 T with SWIFT. 2008; Toronto.
82. Idiyatullin D, Corum C, Moeller S, Garwood M. Gapped pulses for frequency-swept MRI. J Magn Reson 2008;193(2):267-273.
83. Idiyatullin D, Corum C, Moeller S, Prasad HS, Garwood M, Nixdorf DR. Dental magnetic resonance imaging: making the invisible visible. J Endod 2011;37(6):745-752.
84. Idiyatullin D, Corum C, Park JY, Garwood M. Fast and quiet MRI using a swept radiofrequency. J Magn Reson 2006;181(2):342-349.
85. Moeller S, Corum CA, Idiyatullin D, Chamberlain R, Garwood M. Correction of RF pulse distortions in radial imaging using SWIFT. 2008; Toronto. p 229.
86. Powell N, Park J-Y, Garwood M. A New Method for Tailored 2-D Excitation Using Frequency and Gradient Modulation Based on Rapid Passage. 2007; Berlin.
87. Bertero M, De Mol C, Pike ER. Linear inverse problems with discrete data. I. General formulation and singular system analysis. Inverse Problems 1985;1:301-330.
88. Bertero M, De Mol C, Pike ER. Linear inverse problems with discrete data:II. Stability and regularization. Inverse Problems 1988;4:573-594.
89. He B. Modeling & Imaging of Bioelectrical Activity: Principles and Applications: Springer; 2004.
90. Barrett HH, Myers KJ. Foundations of Image Science: John Wiley and Sons; 2004.
91. Van de Walle R, Barrett HH, Myers KJ, Altbach MI, Desplanques B, Gmitro AF, Cornelis J, Lemahieu I. Reconstruction of MR images from data acquired on a general nonregular grid by pseudoinverse calculation. IEEE Trans Med Imaging 2000;19(12):1160-1167.
92. Weiger M, Hennel F, Pruessmann KP. Sweep MRI with algebraic reconstruction. Magn Reson Med 2010;64(6):1685-1695.
93. Hansen PC. Regularization Tools. 4.1; 2008.